Geometry of simulated fractures

V. V. Mourzenko,* J.-F. Thovert, and P. M. Adler*
Laboratoire de Phénoménes de Transport dans les Mélanges, CNRS, Asterama 2, Avenue du Téléport, 86360-Chasseneuil du Poitou, France
and Institut de Physique du Globe de Paris, tour 24, 4 place Jussieu, 75252 Paris Cedex 05, France
(Received 2 October 1995)

The geometry of real fractures is modeled by random surfaces numerically generated. The fracture space and the contact area are determined by the spatial distribution of the upper and lower surfaces. The contact area and the mean aperture are analytically studied. The contact number is calculated for fractures with different height covariance functions. The percolating properties and the structure of the percolating cluster formed in the fracture are determined. [S1063-651X(96)00906-3]

PACS number(s): 64.60.Ak, 91.60.Ba, 02.40.−k, 47.11.+j

I. INTRODUCTION

Experimental and theoretical analyses of hydraulic, transport, and mechanical properties of real fractures in rock have shown that they depend on the geometry of fracture space and surfaces. It has been shown by experiments [1,2] and by direct numerical simulations [3,4] that the flow in a single fracture with rough surfaces occurs through a system of flow paths separated by contact zones. The flux distribution depends on the variance of the fracture aperture probability distribution; the size of the flow channels is determined by the spatial correlation length of the aperture field.

Flow channeling in fractures influences solute transport [1,5]. It was found that the apparent solute dispersion depends on the variance of the aperture distribution [3] and on the mixing between flow channels [6,7].

The models that are usually used in the study of the stress-strain behavior of fractured media include the aperture density distribution and the spatial correlations [8]. The closure of rock joints depends on the fracture surface roughness and the surface topography [9]. The distribution of contacts between fracture surfaces influences the normal joint stiffness [10].

Natural rough surfaces are considered in many studies, but only a few works deal with real fractures. Brown, Kranz, and Bonner [11] measured surface profiles and considered the composite topography of natural rock joints. The composite topography of correlated and uncorrelated rock fractures was studied by Brown and Scholz [12,9]. Aperture measurements were made by Hakami and Barton [13] and spatial correlations of the aperture field were analyzed by Hakami [14]. An exponential model was found to be a good approximation of these correlations. Laboratory measurements of fracture apertures and contact areas were presented by Gale [15]. Some geometric properties of real fractures were studied experimentally by Gentier [2]. It was shown that the experimental variograms of surface profiles at small distances are well described by a Gaussian model.

The model of a fracture as a void volume between two random spatially correlated surfaces was successfully used in various studies. Brown [4,16] numerically analyzed fluid flow and electric conduction in a fracture whose surfaces have normally distributed heights. Closure of a fracture with two rough surfaces was considered by Unger and Mase [17]. The model of a fracture with spatially correlated fractal surfaces was developed by Wang, Narasimhan, and Scholz [18]. A recent paper of Plouraboué *et al.* [19] deals with the aperture of fractures with self-affine surfaces.

To the best of our knowledge, the geometrical properties of fractures have not been systematically studied from a theoretical standpoint, though they represent an interesting problem where several ingredients are intimately mixed. Basically, a fracture is a random two-dimensional structure whose geometry and topology control the flow properties. The two-dimensional character is a crucial simplification in many respects. The properties of excursion sets of random fields [20] can be used to derive the number of contacts between the two surfaces; because of the two-dimensional character, this number is closely related to the connectivity of the open space [21]. The fracture aperture is also a random function of position to which the classical techniques of percolation (cf. [22]) can be applied. Hence this study necessitates the application of a variety of techniques that are gathered here in an unusual manner; in order to make this paper readable by people with different backgrounds, each technique is presented in a relatively detailed way, which may be too long for the specialists. A last important remark is that the results of this study will be compared to experimental data whenever possible.

This paper is organized as follows. Section II is devoted to a general description of the model where fractures are obtained by generating couples of random surfaces. Each surface can be described by its height with respect to a given reference plane. The heights are assumed to be normally distributed with a given standard deviation σ_h. The distance between the average planes of each surface is the mean aperture b_m of the fracture. The heights of one surface may be assumed to be spatially correlated; a particular correlation function has been chosen that contains two parameters: the correlation length l and a characteristic exponent H. Finally, the two surfaces of a given fracture may be correlated one to another; this intercorrelation is characterized by a dimensionless parameter θ. Hence the modelization that is used in this

*Permanent address: Institute for Problems in Mechanics, Russian Academy of Sciences, 101 prospect Vernadskogo, Moscow 117526, Russia.

paper contains four independent parameters b_m/σ_h, l/σ_h, H, and θ. The resulting fractures can be described by a number of macroscopic geometric entities, such as the contact zones, the closed and open fracture volume, and the cyclomatic number of the percolating cluster which are carefully defined in Sec. II. The influence of the four independent parameters on these macroscopic properties will be studied in this paper.

The method of random surface generation with given statistical properties is described. A spatially periodic stochastic field is generated on a unit cell by the method of Fourier transforms. The unit cell of size L is discretized in elementary squares of size a. Thus two additional length scales a and L are introduced in the modelization; since they are artificial in character, they should not influence the macroscopic properties. Because the two surfaces of the fracture cannot overlap, the corresponding Gaussian variables are at a threshold, as they were for reconstructed porous media [23]. This direct analogy can be used to derive some analytical expressions for the mean contact zone area, for the mean fracture volume, and for their variations that are compared with numerical results in Sec. III. Good agreement is obtained for mean values and for variances.

The distribution of contacts between fracture surfaces is analyzed in Sec. IV. For Gaussian random fields with a differentiable covariance, the contact number estimations compare well with the numerical results. The analysis was extended to nondifferentiable covariances. It is shown that for self-affine surfaces the number of finite contact zones depends upon the discretization parameter a/l according to a power law. When the contact area is smaller than a certain critical value, some of the noncontacting zones form the open fracture space that corresponds to the so-called percolating cluster. The connectivity of the cluster is quantified by the first Betti number $\beta_1(A_{\mathrm{PC}})$, i.e., the number of independent cycles. It was found that $\beta_1(A_{\mathrm{PC}})$ is a decreasing function of the correlation length of the aperture field, in the same manner as the contact number.

Percolating properties and the structure of the percolating cluster of the fracture are analyzed in Sec. V. The percolating threshold P_c for the model considered corresponds to ''site'' percolation on a square lattice. It is shown that P_c is a decreasing function of the ratio l/a. For the percolating cluster near the threshold, the critical exponents β, β/ν, and γ are calculated for various parameters of the model.

II. GENERAL

A. Height distribution

Real fractures in rocks are very heterogeneous and irregular in character. Usually, an arbitrary reference plane $z=0$ is introduced and both upper and lower surfaces of the fracture are described by [Fig. 1(a)]

$$z=h^{\pm}(x,y)+h_0^{\pm}, \tag{1}$$

where $h_0^{\pm}$ are the mean planes of each surface. This is a simplification of the problem because a real fracture profile may not be a single-valued function of x and y [Fig. 1(b)]. A detailed analysis of the rock surfaces with a scanning electron microscope showed that overhangs are not prevalent at scales comparable with the resolution of the laboratory profilometer [24]; therefore such cases are not considered here.

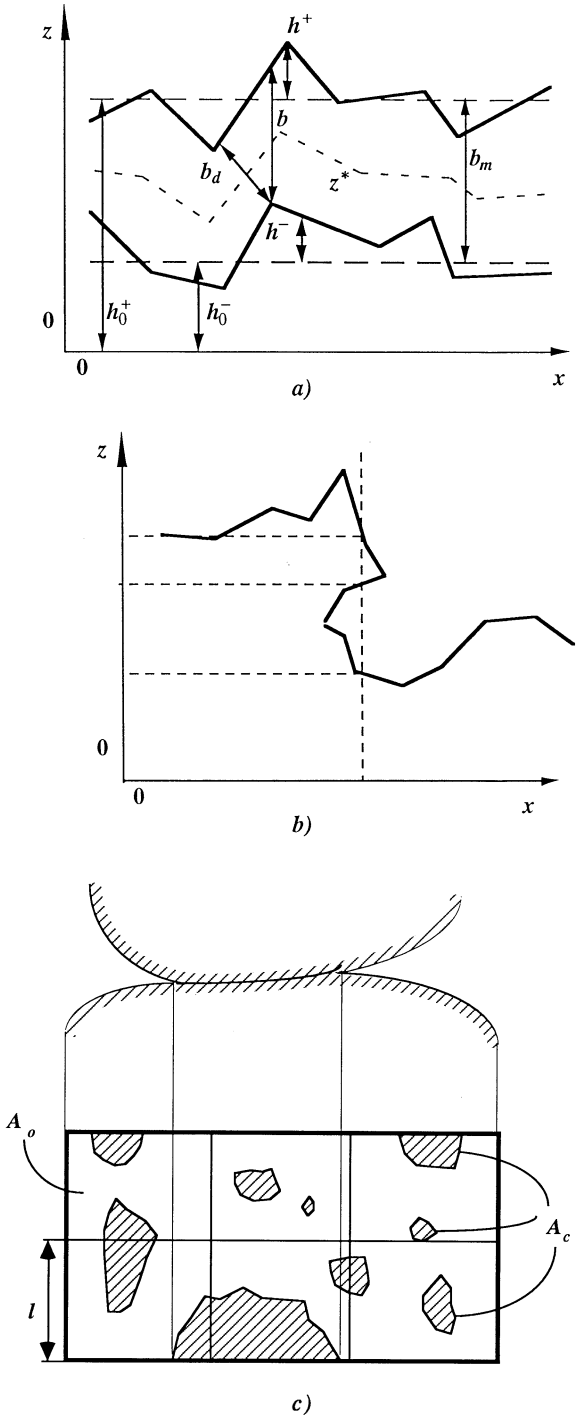

FIG. 1. (a) Conventions and notations for the fracture geometry. (b) Overhanging of a fracture surface profile. (c) Contact area and void area of a fracture. $A/l^2=6$, $N_c=9$, and $n_c=1.5$.

At a given point (x,y), the mean surface z^*, the separation w, and the distance b_m between mean surfaces are defined as

$$z^*=\tfrac{1}{2}(h^+ + h_0^+ + h^- + h_0^-), \tag{2a}$$

$$w=h^+ + h_0^+ - h^- - h_0^-, \tag{2b}$$

$$b_m = \langle w \rangle = h_0^+ - h_0^- , \tag{2c}$$

where $\langle\ \rangle$ denotes the statistical expectation. When b_m decreases, the two surfaces touch one another. In principle, the new shape of the two surfaces after contact occurs could be obtained by taking into account the deformation of the two matrices. However, this phenomenon will not be considered here. Instead, a simplified viewpoint will be adopted [18,4] and the separation b is defined as

$$b = \begin{cases} w, & w(\mathbf{r}) \geqslant 0 \\ 0, & w(\mathbf{r}) < 0. \end{cases} \tag{3}$$

Observation results are often described by a Gaussian distribution [9]

$$\varphi(T) = \frac{1}{\sqrt{2\pi}\sigma_T} \exp\left[-\frac{T^2}{2\sigma_{T^2}} \right], \quad T = h^+, h^- \tag{4}$$

$$\sigma_T^2 = \langle T^2 \rangle,$$

where σ_T is the standard deviation of T; it is supposed that $\langle T \rangle = 0$. This paper will be restricted to such Gaussian height distributions.

When both surfaces are totally separated and do not touch each other, the mean surface z^* and the separation w are also Gaussian functions with standard deviations σ_w and σ_z, which are related to σ_h by

$$\sigma_h^2 = \sigma_e^2 + \tfrac{1}{4}\sigma_w^2, \tag{5}$$

$$\sigma_h = \sigma_h^+ = \sigma_h^- .$$

The upper and lower surfaces of real fractures cannot be considered as statistically independent. Observation of ''mated'' fractures [11] showed that profile heights of both surfaces are correlated over large distances, depending upon the origin of the fracture. Consider the cross covariance

$$\langle h^+ h^- \rangle = \sigma_h^2 - \tfrac{1}{2}\sigma_w^2. \tag{6}$$

If the surfaces are not correlated, it is easy to derive from (6) that

$$\sigma_w^2 = 2\sigma_h^2. \tag{7}$$

In the opposite case of perfect correlation, both surfaces have the same profile and w is constant

$$\sigma_w = 0. \tag{8}$$

The correlation parameter θ may be defined as

$$\theta = \frac{\langle h^+ h^- \rangle}{\sigma_h^2} = 1 - \frac{\sigma_w^2}{2\sigma_h^2}, \quad 0 \leqslant \theta \leqslant 1. \tag{9}$$

The correlation parameter θ widely varies for various types of fractures. Brown and Scholz [12] used totally unmated joints ($\theta = 0$) in closure experiments. In contrast with this, Gentier [2] studied fractures in granite that were in the opposite limit of highly correlated surfaces ($\theta \approx 0.98$). The joints used by Brown, Kranz, and Bonner [11] were characterized by $\theta \approx 0.7$ and 0.94. More detailed information about the correlation of the surfaces may be derived from the spatial cross-covariance function (see Sec. II B).

The separation b is not equal to the local distance b_d between surfaces [Fig. 1(a)] and it is obvious that $b_d \leqslant b$. Here b is called the aperture of the fracture and $\langle b \rangle$ is the mean aperture.

B. Correlations in the fracture plane

Usually, $h^{\pm}$ are homogeneous random functions of x and y. The statistical properties of a random field $T(\mathbf{r})$ are characterized by a probability density $\varphi(T)$ for the statistical distribution of the local values of T and a spatial covariance function $C_T(\mathbf{r},\mathbf{s})$, which is defined as

$$C_T(\mathbf{r},\mathbf{s}) = \langle [T(\mathbf{r}) - \langle T \rangle][T(\mathbf{s}) - \langle T \rangle] \rangle. \tag{10a}$$

If $T(\mathbf{r})$ is a homogeneous and isotropic field, which is often true for fracture surfaces, the covariance function only depends upon the scalar $r = \|\mathbf{r} - \mathbf{s}\|$ ($\|\mathbf{a}\|$ denotes the norm of a vector $\mathbf{a}$),

$$C_T(\mathbf{r},\mathbf{s}) = C_T(r). \tag{10b}$$

The correlation between the upper and lower surfaces can be described by a cross-covariance formula

$$C_h^*(\mathbf{r},\mathbf{s}) = \langle h^+(\mathbf{r}) h^-(\mathbf{s}) \rangle. \tag{11}$$

If $C_{h^{\pm}}$ and C_h^* are known and C_h^* is only a function of r, the covariance functions C_{z^*} and C_w for z^* and w can be found

$$C_{z^*}(r) = (C_{h^+} C_h^*)/2,$$

$$C_w(r) = 2(C_{h^-} C_h^*). \tag{12}$$

Several covariance functions are proposed for fracture surfaces. Whitehouse and Archard [25] used an exponential function

$$C_h = \sigma_h^2 \exp(-r/l), \tag{13}$$

where l is the correlation distance. Experimental measurements of fracture aperture distribution [14,26] showed that spatial correlations of b of a large class of rock fractures may be well approximated by the exponential model.

It is known [20] that a homogeneous random field possesses everywhere a mean-square derivative if and only if the second-order partial derivative of its covariance function exists and is finite at the origin. Since the correlation function (13) displays an angular point at $r = 0$, random fields with this covariance are nondifferentiable in mean square.

If C_h is a Gaussian function,

$$C_h = \sigma_h^2 \exp[-(r/l)^2], \tag{14}$$

the corresponding random fields are continuous and have derivatives in mean square. Both (13) and (14) are particular cases of the general form [27]

$$C_h = \sigma_h^2 \exp[-(r/l)^{2H}], \quad 0 \leqslant H \leqslant 1. \tag{15}$$

The covariance function (15) with $0 < H < 1$ corresponds to self-affine surfaces that remain the same in a statistical sense under an affine transformation in vertical and horizontal di-

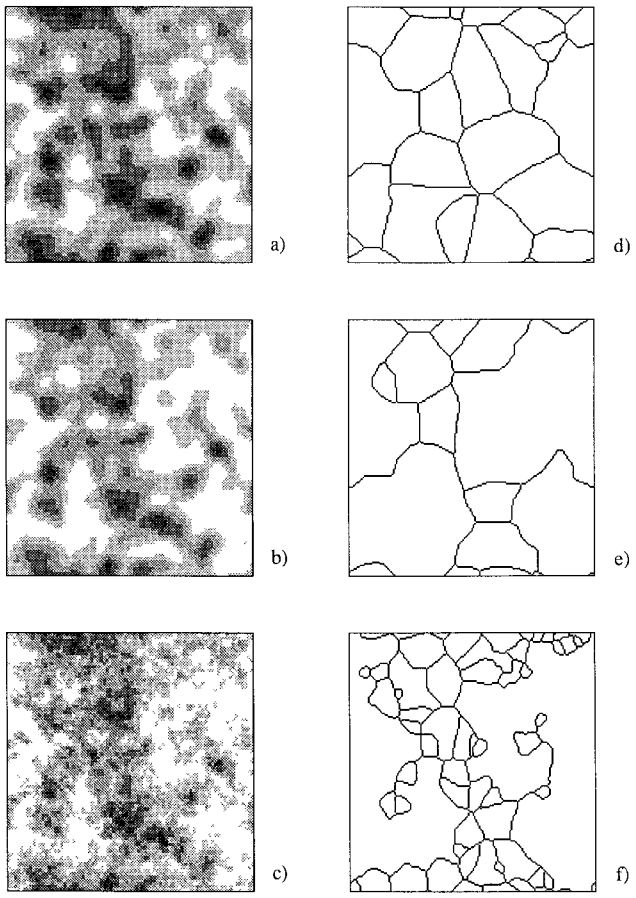

FIG. 2. (a)–(c) Examples of simulated aperture distributions over the fracture plane and (d)–(f) the corresponding graphs of the skeleton of the open fracture space. Six levels of shadings are distinguished from zero (white) to the largest value (dark) of the aperture. The shading steps are equal to $1.25\sigma_h$. Data are for (a) and (d) $b_m/\sigma_h=1$, $H=1$; (b) and (e) $b_m/\sigma_h=0.2$, $H=1$; (c) and (f) $b_m/\sigma_h=0.2$, $H=0.5$.

rections [28]. This form of the covariance function uses the fact that in practice there exists an effective upper cutoff length l for self-affinity, above which all the correlations between surface heights disappear. The parameter H is called the ''roughness exponent'' [29] and it describes the scaling law for self-affine surface heights.

The analysis of power spectra of various natural rock surfaces [24] showed that they verify the power law (15). The self-affine model was successfully used to describe fracture geometry [18,19] and fluid flow; it was also used to study electrical transport [4,16] and hydrodynamic tracer dispersion in fractures [30].

The upper and lower surfaces of the fractures are supposed to be generated with the same spatial correlation distance l; the covariance C_h and the cross covariance C_h^* are described by the general form (15) with the same l as well. This agrees with the results of the laboratory study of well-mated ($\theta\approx0.97$) fractures in granite, where the covariance functions $C_{h\pm}/\sigma_h^2$ and the cross covariance $C_h^*/C_h^*(0)$ were found to be identical [2]. In the opposite limit $\theta=0$, the cross covariance $C_h^*=0$ and the spatial correlations in the fracture plane are completely defined by the covariance functions $C_{h\pm}$. For intermediate values of θ, the real fracture surfaces are shown to be correlated on scales larger than some ''correlation distance'' λ_0 and mismatched at small scales. This can be deduced from the power spectra of the composite topography of fracture surfaces [11]. An analysis of the topography data for Gaussian fractures in quartzite ($\sigma_h\approx4$ μm) and in granite ($\sigma_h\approx1.5$ μm) showed that λ_0 lay within 150–200 and 75–100 μm, respectively [9]. These values are larger than the corresponding correlation distances l for the surfaces: 12–15 and 5–7 μm.

C. Generation of fractures

In order to analyze the fracture geometry, random fields with prescribed statistical properties should be generated. Since only homogeneous Gaussian surfaces are considered here, the problem is restricted to normally distributed variables.

Since it is impossible to generate fields with an arbitrarily large extent, an homogeneous fracture is considered as a two-dimensional spatially periodic medium, composed of identical unit cells of size L, which is supposed to be much larger than the correlation distance l of the generated field. A correlated random Gaussian field can be generated by the method of Fourier transforms, which is recalled by Adler [23]. The numerical grid is composed of $N_L\times N_L$ elementary squares of size $\Delta x=\Delta y=a$; the correlation distance is discretized into n_l such squares, i.e., $l=n_l a$; moreover, $L=N_L a$. At each node ($x_k=ka$, $y_m=ma$), the Gaussian spatially correlated periodic field Y_{km} may be calculated as

$$Y_{km}=N_L\sum_{s,p=0}^{N_L-1}\sqrt{\hat{R}_{sp}}\hat{X}_{sp}\exp\left[-\frac{2\pi i(sk+mp)}{N_L}\right],\qquad k,m=0,\ldots,N_L \quad (16)$$

$$\hat{R}_{sp}=\frac{1}{N_L^2}\sum_{k,m=0}^{N_L-1}C_{km}\exp\left[\frac{2\pi i(sk+mp)}{N_L}\right],\quad s,p=0,\ldots,N_L$$

$$\hat{X}_{sp}=\frac{1}{N_L^2}\sum_{k,m=0}^{N_L-1}X_{km}\exp\left[\frac{2\pi i(sk+mp)}{N_L}\right].$$

C_{km} is the covariance matrix of Y_{km}, which is derived from (10b),

$$C_{km}=C_T(\sqrt{x_k^2+y_m^2}). \quad (17)$$

X_{km} is a noncorrelated standard Gaussian field.

Properties of the mean surface z^* are not analyzed here. The upper and lower surfaces of fractures are supposed to be independently generated ($\theta=0$), but with the same spatial correlation distance l. Because the vertical and lateral coordinates are not connected in the models considered here, it is possible to use different length scales for them. The natural length scale of the vertical coordinate is the standard deviation σ_h; the two horizontal coordinates were normalized by the correlation distance l.

Some examples of generated fields are presented in Fig. 2

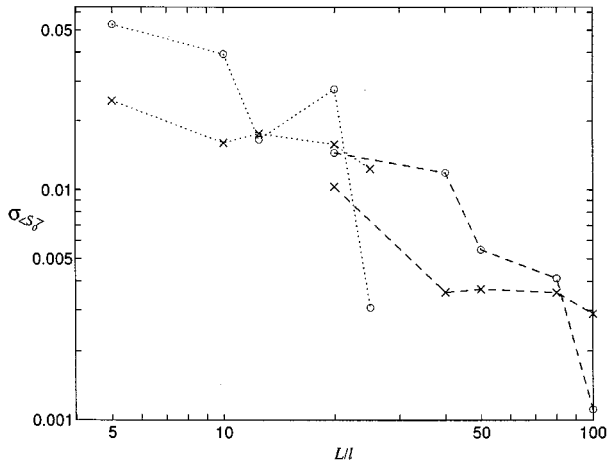

FIG. 3. Standard deviation $\sigma_{\langle S_0\rangle}$ of the mean fractional void area $\langle S_0\rangle$ over N_r realizations for $b_m/\sigma_h=0.2$, $H=0.5$. Data are for $l/a=8$ (dotted lines) and 2 (dashed lines); $N_r=10$ (○), 20 (×).

for various values of b_m and H. For each generated sample, the covariance C_T, defined in (10a), can be estimated as

$$C_T^e(k,m)=\frac{1}{N_L^2}\sum_{s,p=0}^{N_L-1} T_{s,p}T_{s-k,p-m}-\overline{T^2}, \tag{18}$$

$$\overline{T}=\frac{1}{N_L^2}\sum_{s,p=0}^{N_L^2} T_{s,p}, \quad T=h^+,h^-.$$

Due to the finite size of the unit cells, C_T^e may differ from C_T and may vary from one realization of T to another. It was found that for a single realization, C_h^e may differ from the theoretical C_h used in (16) by more than 20% for $x/l\geqslant 1$. When C_h^e was averaged over five realizations, the difference with C_h decreased to 10%.

Tests were performed to find the minimal number of realizations N_r that yields statistically representative results. Various quantities were averaged over N_r realizations and N_r was increased until the mean values were stable. The number of realizations N_r that was needed to obtain significant means depended upon the quantity of interest and the parameters of fractures. In each case, it was defined separately.

It should be noted that the statistical stability of the results depends upon the sample size L/l. For example, Fig. 3 shows the standard deviation $\sigma_{\langle S_0\rangle}$ of the mean value $\langle S_0\rangle$ of the fractional void area of the fracture averaged over different sets of realizations as a function of the parameter L/l. It is clear that $\sigma_{\langle S_0\rangle}$ is a decreasing function of L/l.

D. Terminology

When surfaces are in contact, the area of contact and the number of contact zones are random variables that depend on the statistical properties of surfaces and the mean separation b_m. The contact surface can be described by two variables, namely, the number of contact zones n_c for the area l^2, based on the correlation distance, and the fractional contact area S_c, which is defined as

$$n_c=N_c\frac{l^2}{A}, \tag{19}$$

$$S_c=\frac{A_c}{A}, \tag{20}$$

where A_c is the area of the projection of the total contact surface on the plane $z=0$, A is the cross-sectional area of the fracture plane, and N_c is the total number of contacts over A [Fig. 1(c)].

When the separation b_m is large enough, the contact surface is split into N_c finite contact zones. When b_m decreases, new contact zones appear and the existing ones grow and merge; at some critical value $b_m=b_{mc}$, a contact zone of infinite extent appears, together with some finite contact zones that persist.

Equivalently, the total number N_0 and the number n_0 for the area l^2 of noncontacting zones (or void zones) can be introduced

$$n_0=N_0\frac{l^2}{A}. \tag{21}$$

The fractional void S_0 is defined as

$$S_0=\frac{A_0}{A}=1-S_c, \tag{22}$$

where A_0 is the projection of the total surface of the void volume of the fracture.

When the contact surface is small, most of the noncontacting zones may be gathered into a large percolating cluster, where fluid circulates. The probability P_c of the appearance of such a percolating cluster is called the percolating probability [31].

The ratio S_{PC} between the area of the projection A_{PC} of the surface of the percolating cluster and A is called the fractional area of the percolating cluster

$$S_{\mathrm{PC}}=\frac{A_{\mathrm{PC}}}{A}. \tag{23}$$

A fracture can be partitioned into open and closed spaces depending whether or not a zone with $b>0$ belongs to the percolating clusters. The total number N_0 of void zones includes the number of percolating clusters, which is usually 1, and the number N_0-1 of isolated void zones of finite extent.

Define the average size Z_0 of a finite void zone as

$$Z_0=\frac{\Sigma_{k=1}^{N_0}A_{k0}^2}{\Sigma_{k=1}^{N_0}A_{k0}}, \tag{24}$$

where A_{k0} is the area of the kth isolated void zone. The sums in (24) run only over zones of finite extent and the infinite percolating cluster is excluded. The definition (24) corresponds to the usual definition of the average cluster size [22] used in percolation literature.

When the two surfaces are separated and the contact surface is subdivided into several zones N_c, the percolating cluster may be skeletized and can be reduced to a graph with N_e connecting edges and N_v vertices. This graph can be used as for porous media [32] to characterize the structure of the percolating cluster by the number of independent cycles, i.e., by the first Betti number $\beta_1(A_{\mathrm{PC}})$,

$$\beta_1(A_{\mathrm{PC}})=N_e-N_v+1, \tag{25}$$

where the number of connected components is supposed to be equal to 1.

It should be noted that the number $\beta_1(A_{\mathrm{PC}})$ can be considered as the number of ''holes'' (i.e., of contact zones) in the percolating cluster. It is obvious that $\beta_1(A_{\mathrm{PC}})\leqslant N_c$ because some contacts can be located within void zones of finite size (such as C_1 and C_2 in Fig. 4).

The geometry of a fracture is fully described by the covariance functions C_{z*} and C_w and by the probability densities $\varphi(z^*)$ and $\varphi(w)$. The main goal of this paper is the statistical characterization of the geometry of a fracture. N_r statistical realizations of fractures with fixed values of σ_h, σ_w, l, H, and b_m were generated; then the statistical means of the aperture $\langle b\rangle$, of the fractional areas $S_c, S_0, S_{\mathrm{PC}}$, and of other characteristic quantities were analyzed as functions of these geometrical parameters.

III. GAUSSIAN SURFACES: SOME THEORETICAL RESULTS AND NUMERICAL SIMULATIONS

Some parameters of Gaussian correlated fields, such as the mean aperture, the fractional area, and some others may be estimated analytically. Such estimations are presented here together with results of numerical simulations.

A. The fractional void area

It is convenient to start with the fractional void area S_0. The aperture $b(x,y)$ defined by (3) has a probability density that is simply a truncated Gaussian distribution

$$\varphi^+(b)=\frac{A_b}{\sqrt{2}\pi\sigma_b^*}\exp\left[-\frac{(b-b_m)^2}{2\sigma_b^{*2}}\right],\quad b>0 \tag{26}$$

TABLE I. Standard deviations σ_{S_0} and $\sigma_{\bar{b}}$ of the mean void area S_0 and of the mean aperture $\bar{b}$ estimated numerically and derived from Eqs. (32) and (38). Data are for $H=1$, $b_m/\sigma_h=0.2$, $l/a=4$, and $N_r=50$.

	σ_{S_0}		$\sigma_{\bar{b}}$	
l/L	numerical	theoretical	numerical	theoretical
0.050	0.0338	0.0361	0.0659	0.0740
0.057	0.0431	0.0412	0.0891	0.0845
0.067	0.0496	0.0481	0.1028	0.0987
0.080	0.0626	0.0577	0.1174	0.1184
0.100	0.0742	0.0722	0.1546	0.1479

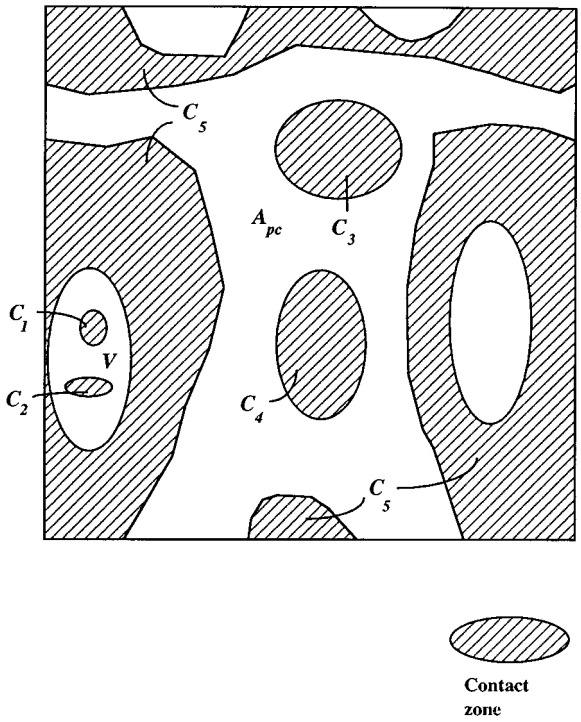

FIG. 4. Distribution of contacts within a fracture. $N_c=5$, $\beta_1(A_{\mathrm{PC}})=3$. Two contacts C_1 and C_2 are contained within a finite void zone V; two contacts of finite extent, C_3 and C_4, are contained within the percolating cluster A_{PC}; C_5 is the only contact zone of infinite extent.

$$\sigma_b^*=\sqrt{2}\sigma_h\quad(\theta=0).$$

Since (26) only describes the case $b>0$, the probability density needs to be renormalized by the constant A_b

$$A_b=\frac{2}{\rho},\quad \rho=\mathrm{erfc}\left(-\frac{b_m}{\sqrt{2}\sigma_b^*}\right). \tag{27}$$

For any realization, S_0 is defined as the average of the phase function B of the void zones

$$S_0=\frac{1}{A}\int_A B(\mathbf{r})d\sigma, \tag{28a}$$

$$B(\mathbf{r})=\begin{cases}1, & w(\mathbf{r})>0\\ 0, & w(\mathbf{r})\leqslant 0.\end{cases} \tag{28b}$$

The random field B, which is derived from a Gaussian field, was used by Adler, Jacquin, and Quiblier [33] to study three-dimensional porous media. It is clear that the statistical properties of B can be derived from those of w. The derivation of the covariance function C_B from C_w is presented by Adler, Jacquin, and Quiblier [33] together with the solution of the inverse problem. Here, only the mean $\langle S_0\rangle$ and the variance of S_0 will be evaluated. $\langle S_0\rangle$ can be estimated as

$$\langle S_0\rangle=\mathrm{Prob}\{w>0\}. \tag{28c}$$

Since w is a standard Gaussian function, $\langle S_0\rangle$ is equal to

$$\langle S_0\rangle = \frac{\rho}{2}. \tag{29}$$

The substitution $b_m=0$ gives the obvious result $\langle S_0\rangle=1/2$.

Results relative to $\langle S_0\rangle$ are presented in Fig. 5(a) for various covariances C_b. Good agreement exists between the theoretical result (29) and the numerical results.

The value of S_0 defined by (28a) is the spatial average of the variable B over the fracture plane A and converges to $\langle S_0\rangle$ only when the sample size L/l tends to infinity. In practice, S_0 is also a random variable and varies from one statistical realization of a fracture to another and the variance $\sigma^2_{S_0}=\langle S_0^2\rangle-\langle S_0\rangle^2$ depends upon the sample size L/l.

So far, only the Gaussian distribution of the heights has been used to find $\langle S_0\rangle$. If the variance of S_0 is to be calculated, the correlation properties in the fracture plane are needed, as illustrated by the following calculations. According to (28), the fluctuations of S_0 are described by the variance

$$\sigma^2_{S_0}=\frac{1}{A^2}\int_A\int_A\langle B(\mathbf{r}_1)B(\mathbf{r}_2)\rangle d\sigma_1 d\sigma_2-\left[\frac{1}{A}\int_A\langle B(\mathbf{r})\rangle d\sigma\right]^2$$

$$=\frac{1}{A}\int_A C_B(\mathbf{r})d\sigma, \tag{30}$$

where C_B is the covariance function of the field $B(\mathbf{r})$ [23]

$$C_B(r)=\langle B(0)B(r)\rangle-\langle B\rangle^2,$$

$$\langle B(0)B(\mathbf{r})\rangle=\int_0^{+\infty}dw_1\int_0^{+\infty}\varphi(w_1,w_2)dw_2, \tag{31a}$$

and $\varphi(w_1,w_2)$ is the joint distribution of two Gaussian variables

$$\varphi(w_1,w_2)=\frac{1}{2\pi\sigma_b^{*2}\sqrt{1-\gamma^2}}\exp\left[-\frac{(w_1-b_m)^2-2\gamma(w_1-b_m)(w_2-b_m)+(w_2-b_m)^2}{2\sigma_b^{*2}(1-\gamma^2)}\right],$$

$$\gamma=\frac{C_w(r)}{\sigma_b^{*2}},\quad \mathbf{r}=\|\mathbf{r}\|. \tag{31b}$$

It is easy to show that, if $C_w(r)$ decreases exponentially when r tends to infinity, $C_B(r)$ also approaches 0. In the limit $l/L\ll 1$ and $b_m/\sigma_b^*\ll 1$, one can obtain from (30)

$$\sigma^2_{S_0}=\left(\frac{l}{L}\right)^2\left[Z_1-\left(\frac{b_m}{\sigma_b^*}\right)^2 Z_2\right], \tag{32}$$

where Z_1 and Z_2 depend only upon H. Formula (32) provides an estimation of the variance of the numerical calculations of the mean value $\langle S_0\rangle$ and illustrates the influence of the sample size on the statistical stability of the numerical simulations (see Table I).

B. Mean aperture

Two possible definitions of the mean aperture $\langle b\rangle$ can be distinguished. The first one $\langle b\rangle_0$ is the mean value over the void fracture area, and the second one $\langle b\rangle$ is taken over the whole surface of the fracture

$$\langle b\rangle_0=\int_0^{+\infty} b\varphi(b)db, \tag{33}$$

$$\langle b\rangle=\langle S_0\rangle\int_0^{+\infty} b\varphi(b)db=\frac{\rho}{2}\langle b\rangle_0, \tag{34}$$

where $\langle b\rangle$ may also be considered as the mean volume $\langle V\rangle$ of a fracture per unit area.

$\langle b\rangle_0$ can be derived from (26)

$$\langle b\rangle_0=b_m+\left(\frac{2}{\pi}\right)^{1/2}\frac{\delta\sigma_b^*}{\rho},\quad \delta=\exp\left(-\frac{b_m^2}{2\sigma_b^{*2}}\right). \tag{35}$$

The statistical averages $\langle b\rangle_0$ and $\langle b\rangle$ can be directly calculated from the numerical realizations of b at one node. In practice, thanks to ergodicity, one can estimate $\langle b\rangle_0$ or $\langle b\rangle$ as the spatial averages $\overline{b_0}$ and $\overline{b}$, defined as

$$\overline{b}=\frac{1}{A}\int_A b(\mathbf{r})d\sigma, \tag{36}$$

$$\overline{b_0}=\frac{1}{A_0}\int_A b(\mathbf{r})d\sigma. \tag{37}$$

These estimations vary from one realization to another with variances $\sigma(\overline{b_0})^2$ and $\sigma(\overline{b})^2$, which can be found in the same way as $\sigma^2_{S_0}$. The variance $\sigma(\overline{b})^2$ can be derived from the joint distribution $\varphi(w_1,w_2)$ of two Gaussian variables in the limit $l/L\ll 1$ and $b_m/\sigma_b^*\ll 1$,

$$\sigma(\overline{b})^2=\langle\overline{b^2}\rangle-\langle b\rangle^2=\left(\frac{l}{L}\right)^2\left[Z_3-\left(\frac{b_m}{\sigma_b^*}\right)Z_4\right], \tag{38}$$

where Z_3 and Z_4 depend only on H. The estimation of $\sigma(\overline{b_0})^2$ may be written as

$$\sigma(\overline{b_0})^2=\frac{4}{\rho^2}\sigma(\overline{b})^2. \tag{39}$$

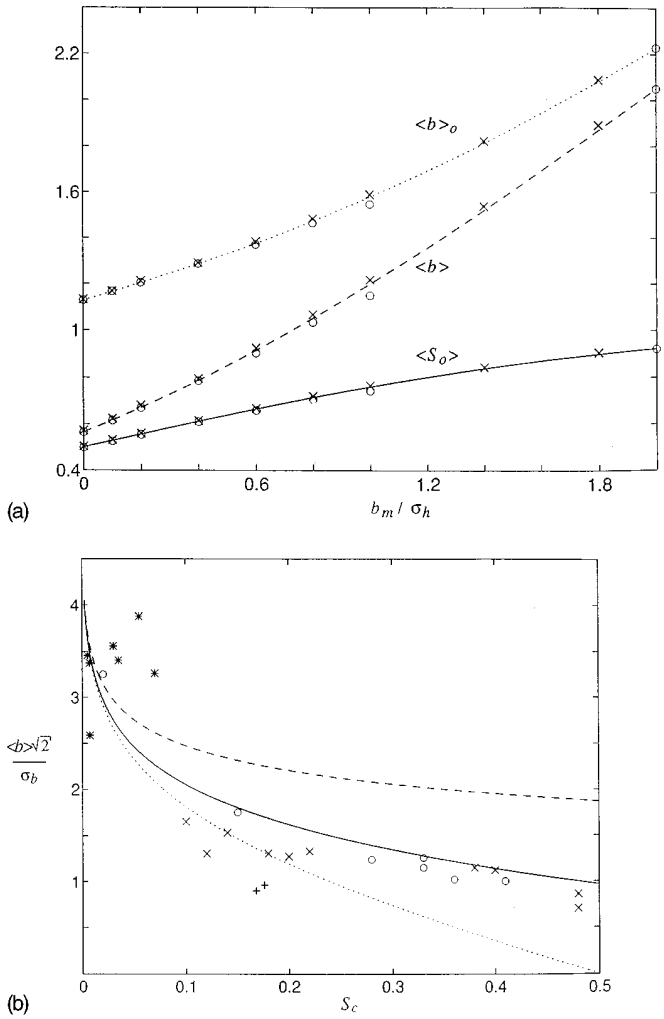

FIG. 5. Mean fractional void area $\langle S_0 \rangle$ [solid line; Eq. (29)], the mean aperture $\langle b \rangle$ [dashed line; Eq. (34)], and the mean aperture $\langle b \rangle_0$ [dotted line; Eq. (35)] of a fracture as functions of b_m/σ_h. Data are for $l/a=1.25$, $N_L=40$, and $H=0.5$ ($\times$); $l/a=4$, $N_L=80$, and $H=1$ ($\bigcirc$). The numerical data are given by ($\times$ and $\bigcirc$). (b) Ratio $\langle b \rangle \sqrt{2}/\sigma_b$ (solid line) as a function of the mean fractional contact area $\langle S_c \rangle$. The dotted line corresponds to $b_m\sqrt{2}/\sigma_b^*$ and the dashed one to $\langle b \rangle_0 \sqrt{2}/\sigma_{b0}$. The experimental data of Hakami [14] are denoted by $\bigcirc$ (drill core sections measurements) and $\times$ (borehole photographs). The data of Hakami and Larsson [26] and Gale [15] are denoted by * and +, respectively.

Figure 5(a) shows $\langle b \rangle_0$ and $\langle b \rangle$ vs b_m. All the numerical estimates are in good agreement with the theoretical predictions.

The formula (38) shows the influence of the sample size on the dispersion of the spatial average b around the statistical average $\langle b \rangle$. The theoretical predictions given by (38) are in good agreement with the numerical estimations in Table I.

Equations (29) and (34) yield a relation between $\langle S_0 \rangle$, $\langle b \rangle$, and $\langle b \rangle_0$. Figure 5(b) shows $\langle b \rangle \sqrt{2}/\sigma_b$ as a function of $\langle S_c \rangle$, where σ_b^2 is the variance of b over the fracture plane

$$\sigma_b^2 = \langle b^2 \rangle - \langle b \rangle^2 = \frac{\rho}{2}\,(b_m^2 + \sigma_b^{*2}) + \frac{\delta b_m \sigma_b^*}{\sqrt{2\pi}} - \langle b \rangle^2. \quad (40)$$

The standard deviation σ_b is used instead of the model parameter σ_b^* because it can be estimated directly in experiments. The dependences $b_m\sqrt{2}/\sigma_b^*$ and $\langle b \rangle_0 \sqrt{2}/\sigma_{b0}$ on $\langle S_c \rangle$ are presented in Fig. 5(b).

When the fractional contact areas S_c are small ($S_c<0.01$), the ratio $\langle b \rangle \sqrt{2}/\sigma_b$ rapidly varies with S_c. In this range of parameters, S_c depends on the distribution of the highest asperities of the fracture surfaces, which correspond to the tail of the height probability density $\varphi(h)$ (4); hence S_c is expected to vary largely from one fracture sample to another.

For large S_c ($S_c>0.2$) the ratio $\langle b \rangle \sqrt{2}/\sigma_b$ decreases slightly with increasing S_c. This means that S_c is sensitive to the minimal nonzero aperture that can be measured in the experiment. The ratio $\langle b \rangle \sqrt{2}/\sigma_b$ is larger than 1 for $S_c<0.48$, while the parameter $b_m\sqrt{2}/\sigma_b^*$ tends to 0 when S_c approaches 0.5.

For comparison purposes, the experimental data are presented in the same plot. The first two data sets of Hakami [14] were obtained by two different types of measurements of the aperture distribution in a single fracture within a quartz sample. The third one was presented by Hakami and Larsson [26]. Two data points represent the experimental results of Gale [15]. Good agreement between all experimental data and the theoretical predictions of the theory was obtained. It should be noted that the data of Hakami and Larsson [26] for fracture with small S_c are scattered around the theoretical curve; this can be explained by the sensibility of S_c to the distribution of the highest surfaces asperities, which varies substantially from one fracture sample to another, as already mentioned.

IV. DISTRIBUTION OF CONTACTS BETWEEN FRACTURE SURFACES

Mechanical properties of real fractures mostly depend on the distribution of contacts between fracture surfaces and their area. The number of contacts and the mean area of a contact zone are analyzed as well as the number of closed zones with nonzero aperture for simulated fracture surfaces with various values of correlation distances. Before the simulation results are discussed, some theoretical concepts are presented.

A. Theory

The number N_c of contacts or the number n_c of contacts per area l^2 for two surfaces [cf. (19)] with normally distributed heights can be considered as the number of zones where the Gaussian random field $F=b_m-w$ with zero mean and standard deviation σ_b^* has values $F>b_m$. If F is a two-dimensional field, the number of N_F of zones with $F>u$ in a set A may be estimated from the value of the differential topology characteristic N_χ of F [20]. Briefly, N_χ is

$$N_\chi = \chi_1 - \chi_0, \quad (41)$$

where χ_1 and χ_0 are the total number of points $(x,y) \in A$ that satisfy [see Fig. 6(a)]

$$\begin{aligned} \chi_1: &\quad F=u,\ F'_x=0,\ F'_y>0,\ F''_{xy}<0; \\ \chi_0: &\quad F=u,\ F'_x=0,\ F'_y>0,\ F''_{xy}>0. \end{aligned} \quad (42)$$

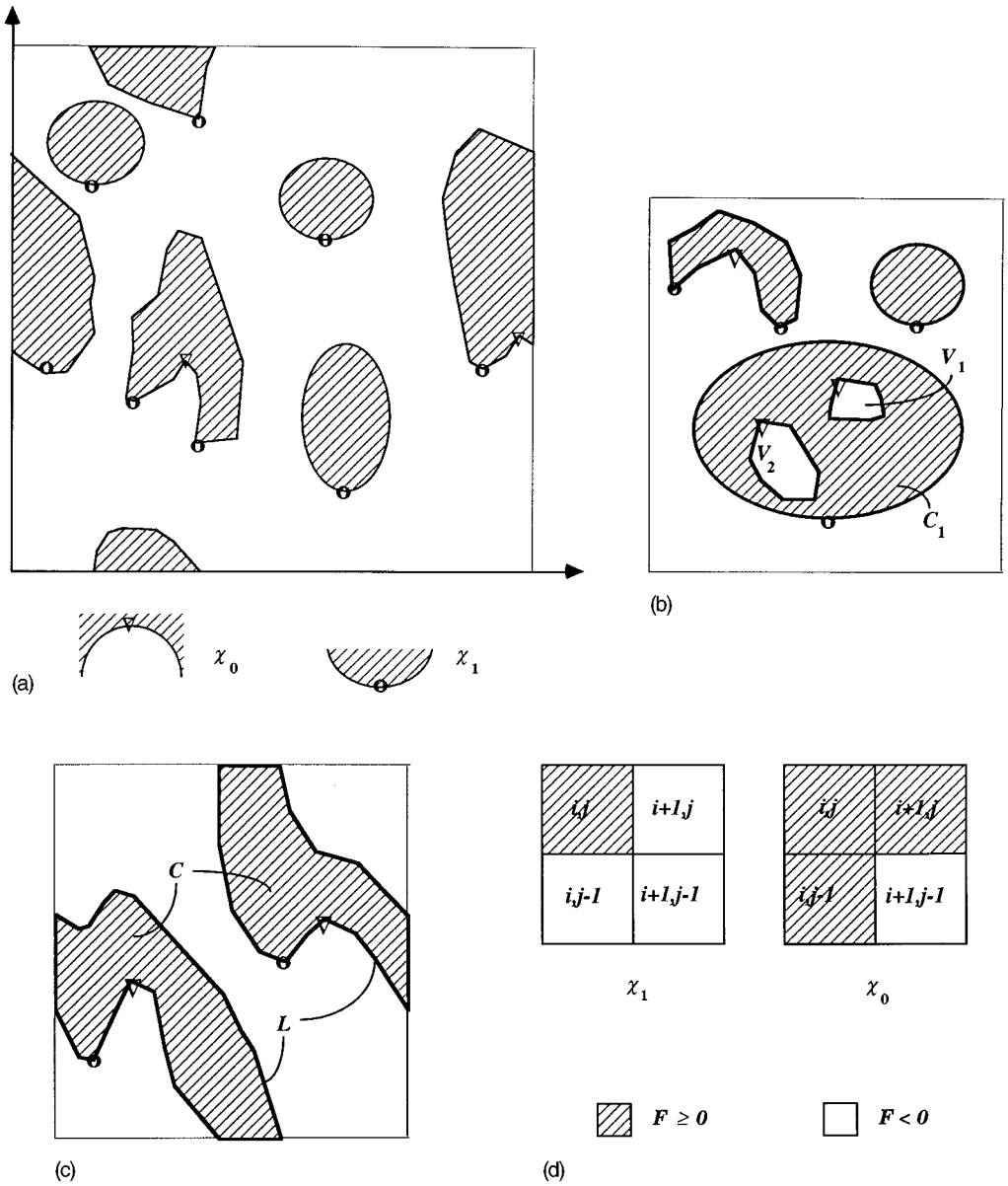

FIG. 6. (a) Differential topology characteristic N_χ of the shadowed contact zone. $\chi_1=8$, $\chi_0=2$, $N_\chi=6$, and $N_c=6$. (b) Contact zone C_1 contains two isolated void zones V_1 and V_2. $\chi_1=4$, $\chi_0=3$, $N_\chi=1$, and $N_c=3$. (c) Infinite contact zone C bounded by the infinite line L. $\chi_1=2$, $\chi_0=2$, $N_\chi=0$, and $N_c=1$. (d) Configurations that contribute to the discrete analog of the differential topological characteristic N_χ.

Equation (41) gives the number of connected contact zones of finite extent that do not contain any void area or are not part of a contact zone of infinite extent. If any contact zone contains some ''holes,'' each hole lowers N_χ by 1 [Fig. 6(b)]. The outer boundary of a periodic infinite contact zone does not contribute to N_χ [Fig. 6(c)].

Generally, N_χ, N_c, and N_0 are related by

$$N_\chi=(N_c-N_c^\infty)-(N_0-N_0^\infty), \tag{43}$$

where N_c^∞ and N_0^∞ are the numbers of contact zones and of void areas of infinite extent. It is clear that

$$N_\chi \leqslant N_c \tag{44}$$

and the formula (41) provides a lower bound of the contact number N_c.

The differential topology characteristic N_χ of the fracture space is also related to the Betti numbers of the void zone and of the contact zone of the fracture (Fig. 7). The void zone of the fracture can be reduced to a topologically equivalent network of edges and vertices. This network or graph is composed of some connected components whose number is called the zeroth Betti number $\beta_0(A_0)$. The first Betti number $\beta_1(A_0)$ (or the cyclomatic number of the void zone) is equal to the number of independent cycles of the graph

$$\beta_1(A_0)=N_e-N_v+\beta_0(A_0), \tag{45}$$

where N_e and N_v are the number of edges and vertices of the graph, respectively. It is obvious that any independent cycle of finite extent encloses one finite isolated contact zone (cf. the cycle $ABEA$ in Fig. 7) and that the numbers of these finite cycles and of those finite contact zones are always equal.

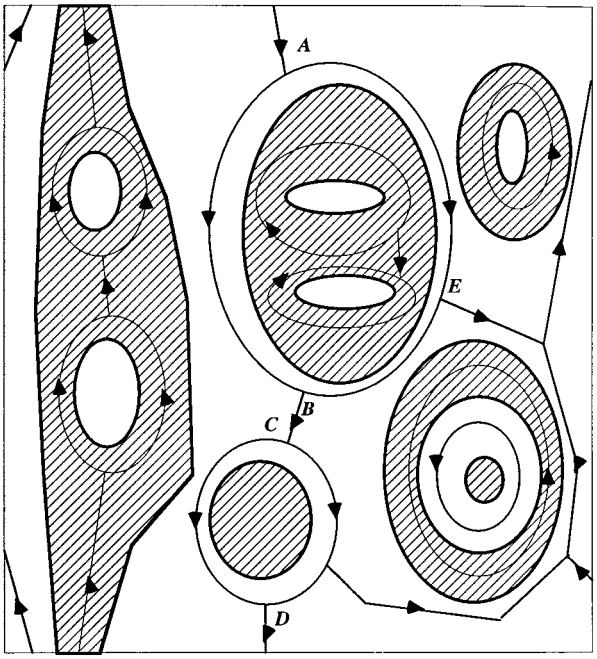

FIG. 7. Graphs of the void (bold lines) and contact (thin lines) zones of the fracture. Contact zones are shadowed.

If a void zone of infinite extent exists, it contains one infinite cycle at least (see the cycle $ABCDA$ in Fig. 7). The correspondence between the numbers of infinite independent cycles and of contact zones of infinite extent depends on the topological structure of the fracture space. If a contact zone and a void zone of infinite extent exist, each contact zone may be enclosed by one and only one independent cycle of the graph of the void zone. When all contact zones are finite, the infinite cycle of this graph does not correspond to any contact zone. In the opposite limit where only finite void zones exist, the corresponding graph consists of some number of finite cycles and the Betti number $\beta_1(A_0)$ is equal to the number of isolated contact zones that are located within the finite void zones.

In general, the total number of contacts N_c is related to the Betti number $\beta_1(A_0)$ of the graph of the void zone of the fracture by

$$N_c=\beta_1(A_0)-N_0^{\infty}+N_c^{\infty}. \tag{46a}$$

A relation dual to (46a) can be derived for the number N_0 of void zones and the first Betti number $\beta_1(A_c)$ of the graph of the contact zone of the fracture

$$N_0=\beta_1(A_c)-N_c^{\infty}+N_0^{\infty}. \tag{46b}$$

In order to obtain a relationship between N_χ and the Betti numbers of the graphs of void and contact zones of the fracture, Eq. (43) can be used. It is obvious that the numbers N_c^{∞} and N_0^{∞} of contact zones and void zones of infinite extent are equal to the numbers $\beta_0^{\infty}(A_c)$ and $\beta_0^{\infty}(A_0)$ of connected infinite components of the corresponding graphs. Finally, N_χ is expressed as

$$N_\chi=\beta_1(A_0)-\beta_1(A_c)-\beta_0^{\infty}(A_0)+\beta_0^{\infty}(A_c). \tag{47}$$

In (46) and (47), it is assumed that any finite contact zone (void zone) is enclosed in a cycle in A_0 (A_c). In particular, these results do not apply when neither A_0 nor A_c percolates.

Consider the case when only one percolating void zone exists. The number

$$N_0^c=N_0-N_0^{\infty}=N_0-1 \tag{48}$$

in (43) is equal to the number of isolated void zones that correspond to the closed porosity of the fracture. The first term $N_c-N_c^{\infty}$ in (43) is the number of isolated contacts. If the fracture is far from the percolation threshold, most contacts are contained in the infinite void zone and $N_c-N_c^{\infty}$ is close to $\beta_1(A_{\mathrm{PC}})$, the cyclomatic number of the percolating cluster. Finally,

$$N_\chi \geqslant \beta_1(A_{\mathrm{PC}})-N_0^c. \tag{49}$$

According to Adler [20], the average $\langle N_\chi\rangle$ over A is given by

$$\langle N_\chi\rangle \approx \frac{\mu(A)\sqrt{|\Delta|}}{(2\pi)^{3/2}}\frac{u}{\sigma_T^3}\exp\left[-\frac{u^2}{2\sigma_T^2}\right],$$

$$\Delta=\left\{\frac{\partial^2 C_F}{\partial x^2}\frac{\partial^2 C_F}{\partial y^2}-\left(\frac{\partial^2 C_F}{\partial x\,\partial y}\right)^2\right\}_{x,y=0}, \tag{50}$$

where $\mu(A)$ is the area of A. If the spatial correlation is given by the Gaussian covariance C_w (14), the random field w will be almost surely continuous, together with its partial derivatives $\Delta=(2\sigma_b^*)^2$ and $\mu(A)=(L/l)^2$; $\langle N_\chi\rangle$ can be deduced from (50),

$$\langle N_\chi\rangle=\left(\frac{L}{l}\right)^2\frac{b_m}{\pi\sqrt{2\pi}\sigma_b^*}\exp\left[-\frac{b_m^2}{2\sigma_b^{*2}}\right]. \tag{51}$$

B. Comparison with numerical data for Gaussian fractures ($H=1$)

Figure 8 shows results of numerical computations of the contact number n_c for an area l^2 when the sample size L/l is varied. It is found that for a fixed value of the discretization ratio a/l, n_c approaches some limit value n_c^{∞} when $L/l\to\infty$. In each series of calculations with fixed a/l, the variations of n_c about n_c^{∞} do not exceed 10% when $L/l\geqslant 10$. The statistical variations of n_c increase if the mean size D_c of a contact zone approaches the sample size. Table II contains the relative standard deviation σ_{n_c}/n_c of the contact number and the inverse mean size of a contact zone obtained numerically as $D_c=\sqrt{S_c/n_c}$, for various values of b_m/σ_h and fixed L/l. It can be seen that when l/D_c approaches $l/L=0.05$, the statistical variance of the contact number increases.

Figure 8 shows that the limit value n_c^{∞} varies with the discretization ratio a/l. In order to analyze the influence of a/l, the contact number n_c is plotted in Fig. 9 for a fixed L/l as a function of a/l. It is clear that for a large enough sample size $L/l=20$ (curve 3), n_c rapidly approaches some limit value n_c^0. In the case $L/l=5$ (curve 1), n_c diverges with decreasing a/l due to a too small sample size that is comparable to the contact zone mean size $D_c\approx 5l$ (see Table II). The variations of n_c^0 obtained by a linear extrapolation of the numerical results (see Fig. 9) with fixed L/l and decreasing

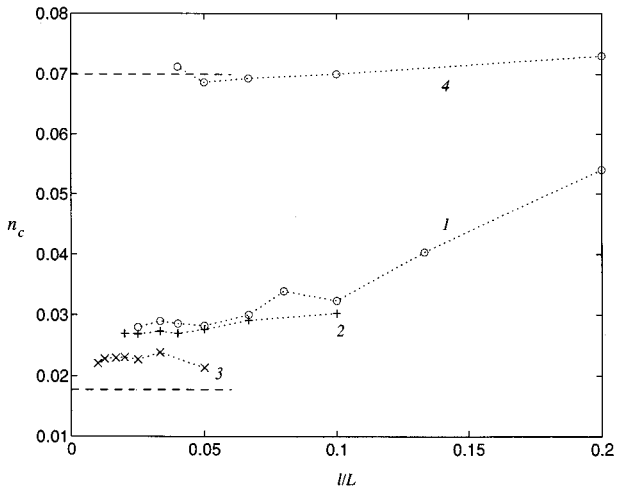

FIG. 8. Contact number n_c for an area l^2 as a function of the ratio l/L of the correlation distance l and of the sample size L for fixed values of a/l. Data are for $H=1$, $b_m/\sigma_h=0.2$, $a/l=0.125$ (1), 0.25 (2), 0.5 (3), and $b_m/\sigma_h=1$, $a/l=0.125$ (4). The dashed lines correspond to the theoretical values given by Eq. (51). The number of realizations is $N_r=100$ for the smallest l/L and 200 for the largest one.

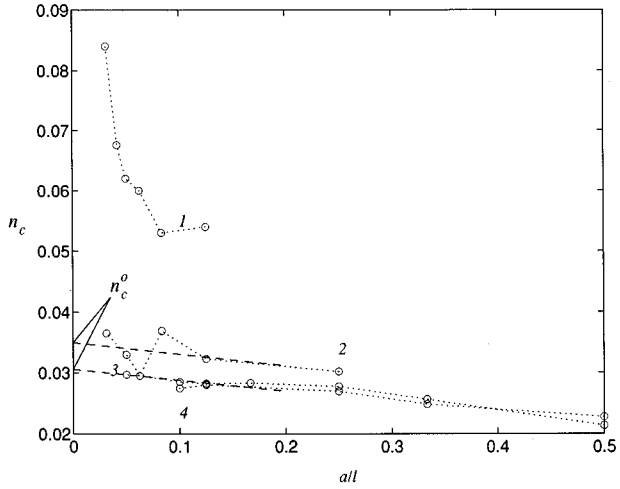

FIG. 9. Contact number n_c as a function of the discretization ratio a/l for $H=1$, $b_m/\sigma_h=0.2$, and a fixed value of l/L. Data are for $l/L=0.2$ (1), 0.1 (2), 0.05 (3), and 0.025 (4).

a/l are illustrated in Table III. It can be seen that, when the sample size L/l is increased, n_c^0 tends toward 0.031. Table III and Fig. 8 show that sample size effects disappear for $L/l \geqslant 20$. The limit values n_c^∞ and n_c^0 obtained in numerical simulations differ from the theoretical predictions given by (51) only for $b_m/\sigma_h \to 0$, as can be seen in Fig. 10.

The difference between $\langle N_\chi \rangle$ and $\langle n_c \rangle$ can be explained by using the formula (43). When $b_m/\sigma_h \gg 1$ the number N_0^c of isolated void zones vanishes, $N_c^\infty=0$, the ratio $(N_0-N_0^\infty+N_c^\infty)/N_c$ tends to 0, and N_χ approaches N_c. In the limit $b_m/\sigma_h=0$, the ratio $(N_0-N_0^\infty+N_c^\infty)/N_c$ is finite and the term $N_0-N_0^\infty+N_c^\infty$ cannot be neglected in (43). It means that for low b_m/σ_h the formula (51) cannot be used for the estimation of $\langle n_c \rangle$.

It may be concluded that for $b_m/\sigma_h \geqslant 0.7$, $\langle N_\chi \rangle$ as derived from (51) gives a good approximation for $\langle n_c \rangle$, while for $b_m/\sigma_h \leqslant 0.7$, the difference between (51) and the estimated value of $\langle n_c \rangle$ increases with decreasing b_m/σ_h. An increase of the sample size L/l does not decrease this difference.

TABLE II. Mean area of a connected contact zone S_c/n_c, the inverse mean size of a contact zone $D_c=\sqrt{S_c/n_c}$, and the relative standard deviation of the contact number σ_{n_c}/n_c as functions of b_m/σ_h. Data are for $H=1$, $L/l=20$, and $l/a=8$. The estimations are derived from Eqs. (27), (29), and (51).

	S_c/n_c		$l/D_c=l\sqrt{n_c/S_c}$		σ_{η_c}/n_c
b_m/σ_h	calculated	theory	calculated	theory	calculated
0.0	25.51	∞	0.20	0	0.39
0.1	20.07	52.68	0.22	0.14	0.41
0.2	15.82	24.96	0.25	0.20	0.36
0.4	9.58	11.26	0.32	0.30	0.29
0.6	6.08	6.82	0.41	0.38	0.20
0.8	4.39	4.67	0.48	0.46	0.17
1.0	3.20	3.43	0.56	0.54	0.15
1.4	2.08	2.09	0.69	0.69	0.12
2.0	1.13	1.19	0.94	0.92	0.13

C. Numerical data for self-affine fractures ($H<1$)

Because of the fractal character of these fractures, a different asymptotic behavior is expected. The convergence of n_c when L/l is increased is illustrated for $H=0.5$ in Fig. 11. It can be seen that n_c reaches n_c^∞ more rapidly than in the case $H=1$ (Fig. 8). A good estimation of n_c^∞ can be obtained with $L/l \geqslant 5$, instead of 20 for $H=1$.

Another obvious difference between the cases $H=0.5$ and 1 is that for $H=0.5$, n_c strongly depends on the discretization ratio a/l for fixed L/l. Figure 12 displays a log-log plot of n_c as a function of l/a for a fixed ratio L/l and various values of H. The number of contacts n_c was found to be approxi-

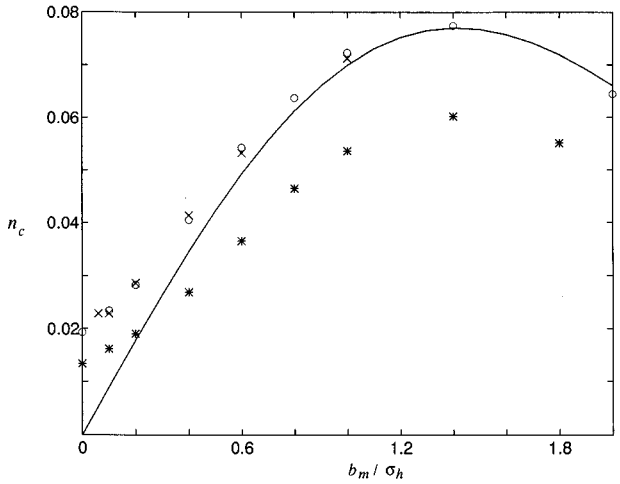

FIG. 10. Contact number n_c as a function of b_m/σ_h. Data are for $H=1$, $a/l=0.125$, and $l/L=0.05$ (○), 0.04 (×); $H=0.5$, $a/l=0.8$, and $l/L=0.031\,25$ (∗). The solid line corresponds to Eq. (51) for N_χ.

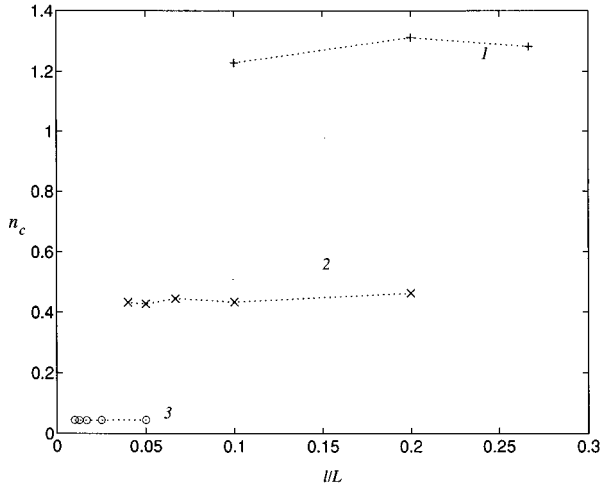

FIG. 11. Contact number n_c as a function of l/L for $H=0.5$ and fixed a/l. Data are for $b_m/\sigma_h=0.2$ and $a/l=0.0625$ (1), 0.125 (2), and 0.5 (3).

mately constant only for $H=1$. It can be seen that n_c follows a power law

$$n_c \propto \left(\frac{l}{a}\right)^s. \tag{52}$$

The exponent s depends upon H and upon b_m/σ_h, as shown in Fig. 13.

In order to estimate s, consider the discrete analog of the differential topology characteristic N_χ (41), where χ_1 and χ_0 are the total numbers of nodes (x_i, y_j), which satisfy [see Fig. 6(d)]

$$\chi_1: \quad F(x_i,y_j)\geqslant u,\ F(x_{i+1},y_j)<u, \tag{53}$$

$$F(x_i,y_{j-1})<u,\ F(x_{i+1},y_{j-1})<u;$$

$$\chi_0: \quad F(x_i,y_j)\geqslant u,\ F(x_{i+1},y_j)\geqslant u,$$

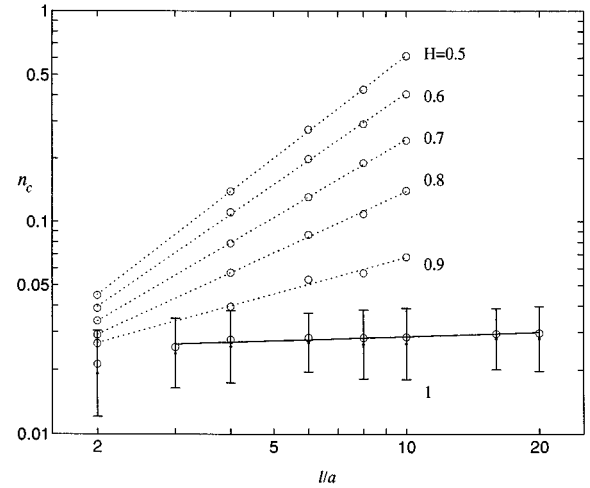

FIG. 12. Contact number n_c as a function of l/a for $b_m/\sigma_h=0.2$, $N_r=100$, $l/L=0.05$, and various values of H. The straight lines are the mean-square fits. The error bars represent the standard deviation interval for the mean value.

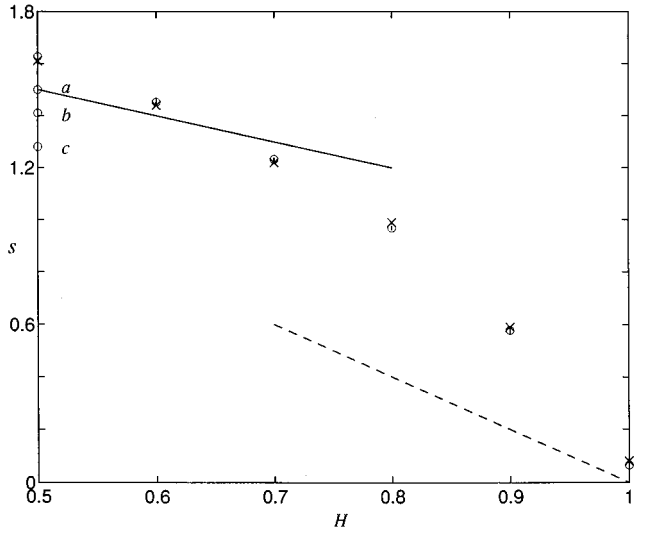

FIG. 13. Scaling exponent $s(\bigcirc)$ for the contact numbers n_c and μ $(\times)$ for the cyclomatic number $\beta_1(A_{\rm pc})$ as functions of H for $b_m/\sigma_h=0.2$. The solid line corresponds to (58), the dashed line to (57). For $H=0.5$, data are for $b_m/\sigma_h=0.4$ (a), 0.6 (b), and 1 (c).

$$F(x_i,y_{j-1})\geqslant u,\ F(x_{i+1},y_{j-1})<u.$$

This can be easily related to Fig. 6(a) when Fig. 6(d) is rotated by an angle of $-\pi/4$.

The mean numbers $\langle\chi_1\rangle$ and $\langle\chi_0\rangle$ can be estimated as

$$\langle\chi_1\rangle=\left(\frac{L}{a}\right)^2 P_1,\ \langle\chi_0\rangle=\left(\frac{L}{a}\right)^2 P_0, \tag{54}$$

where P_1 and P_0 are the probabilities of the configurations displayed in Fig. 6(d). The probabilities P_1 and P_0 are expressed by using the joint probability of the four Gaussian correlated variables x, y, z, and t:

$$P_1=\int_u^{+\infty} dt \int_{-\infty}^{u} dx \int_{-\infty}^{u} dy \int_{-\infty}^{u} f(x,y,z,t)\,dz, \tag{55}$$

$$P_0=\int_u^{+\infty} dt \int_{u}^{+\infty} dx \int_{u}^{+\infty} dy \int_{-\infty}^{u} f(x,y,z,t)\,dz,$$

TABLE III. Extrapolated values of the contact number n_c^0 in the limit $a/l\to 0$ for various L/l. Data are for $H=1$ and $b_m/\sigma_h=0.2$.

L/l	n_c^0
10	0.0350
20	0.0308
25	0.0302
30	0.0296
40	0.0306
theory	0.0178

$$f=\left\{4\pi^2(1-\gamma_2^2)\left[1-\left(\frac{2\gamma_1}{1+\gamma_2}\right)^2\right]^{1/2}\right\}^{-1}$$

$$\times\exp\left\{-\frac{(x+y)^2-\dfrac{4\gamma_1}{1+\gamma_2}(x+y)(t+z)+(t+z)^2}{4(1+\gamma_2)\left[1-\left(\dfrac{2\gamma_1}{1+\gamma_2}\right)^2\right]}\right.$$

$$\left.-\frac{(x-y)^2+(t-z)^2}{4(1-\gamma_2)}\right\},$$

$$t=F(x_i,y_j),\quad x=F(x_{i+1},y_j),$$

$$y=F(x_i,y_{j-1}),\quad z=F(x_{i+1},y_{j-1}),$$

$$\gamma_1=\frac{C_w\left(\dfrac{a}{l}\right)}{\sigma_b^{*2}},\quad \gamma_2=\frac{C_w\left(\sqrt{2}\,\dfrac{a}{l}\right)}{\sigma_b^{*2}}.$$

All the integrals in (55) can be estimated in the limit $a/l\to 0$, and the average $\langle\chi_1-\chi_0\rangle$ per unit area is given by

$$\langle\chi_1-\chi_0\rangle\approx\left(\frac{a}{l}\right)^{2-2H}\frac{2^{H-1}b_m}{\pi\sqrt{2\pi}\sigma_b^*}\exp\left[-\frac{b_m^2}{2\sigma_b^{*2}}\right]. \quad (56)$$

In the limit $H=1$, this formula is identical to (51). According to (56), the scaling exponent s is

$$s=2-2H. \quad (57)$$

This dependence is presented in Fig. 13. The comparison with the numerical results show that (57) provides an estimate that is systematically too low. It should be recalled that the topological characteristic N_χ only gives a lower limit of the contact number according to (44). This is especially important for $H<1$, where the generated surfaces are self-affine fractals (on scales $x<l$) and their cross sections are also fractals [31]. One may suppose that with decreasing values of a/l, the number of holes in the contact zones increases as well as the difference between N_c and $\chi_1-\chi_0$.

Whitehouse and Archard [25] measured the number N_p of peaks detected on a given length of a random surface profile by using various sampling intervals a/l. They found that for the profiles with normally distributed heights and the exponential covariance (13), N_p was inversely proportional to a/l. The scaling law (52) with the exponent s given by (57) for $H=0.5$ also predicts that n_c varies as $(a/l)^{-1}$.

The relation (52) is a consequence of the fact that for $H<1$ the fracture surfaces are self-affine objects. A horizontal section of the surface defines coastlines that are self-similar fractals with a fractal dimension [31]

$$d_c=2-H. \quad (58)$$

Mandelbrot [34] showed that in a plane section, the number of islands having an area greater than a prescribed size l varies as l^{-d_c}. The relation (58) is also displayed in Fig. 13.

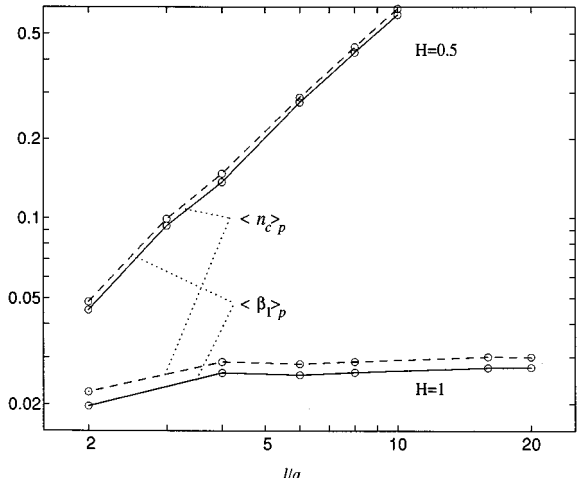

FIG. 14. Mean cyclomatic number $\langle\beta_1 l^2/A\rangle_p$ (solid lines) and the mean contact number $\langle n_c\rangle_p$ (dashed lines) averaged over percolating fractures as functions of l/a for $b_m/\sigma_h=0.2$, $l/L=0.05$, and $N_r=100$.

D. Connectivity of percolating fractures

The number of contacts N_c is related to the cyclomatic number $\beta_1(A_0)$ of the graph of the void volume of a fracture by (46). Let us consider another topological characteristic of this volume, namely, the cyclomatic number $\beta_1(A_{\rm PC})$ of the percolating cluster of the fracture [cf. (25)].

In order to analyze the structure of percolating clusters for each realization of the fracture space, the two-dimensional aperture field is reduced to a graph by a method of conditional thining [32]. Some examples of such graphs are shown in Fig. 2. The graph can be characterized by the number N_e of edges and the number N_v of junctions (or vertices). When N_e and N_v are known, it is easy to calculate $\beta_1(A_{\rm PC})$ (also shortened as β_1) from (25).

Figure 14 displays $\langle\beta_1 l^2/A\rangle_p$ and $\langle n_c\rangle_p$ vs l/a for $H=0.5$ and 1, where $\langle n_c\rangle_p$ is only averaged over the percolating realizations of the fractures. The main observation is that the cyclomatic number β_1 is close to the total contact number N_c. This means that most contacts between two fracture surfaces are in the interior of the percolating cluster (if it exists) and that only a small number of contacts is distributed within closed parts of the void volume of the fracture.

As can be seen from Fig. 14, the cyclomatic number β_1 is given by the power law

$$\langle\beta_1\rangle_p\frac{l^2}{A}\sim\left(\frac{l}{a}\right)^{-\mu}, \quad (59)$$

where the exponent μ depends upon H and b_m/σ_h. Figure 13 displays μ calculated for various H together with the exponent s; it is obvious that $\langle\beta_1 l^2/A\rangle$ and $\langle n_c\rangle$ obey the same scaling law. μ is a decreasing function of b_m/σ_h; the values of μ are very close to the corresponding values of s.

V. STRUCTURE OF PERCOLATING CLUSTERS

When the separation b_m between the two surfaces increases, the total void fracture area grows; when b_m is larger than a certain critical value, most of this surface is connected

over the entire fracture plane and forms a percolating cluster. For finite samples of simulated fractures, various criteria can be chosen to determine whether or not a fracture is percolating [32]. Here a cluster is defined as percolating if a fluid can pass through it from one end to another. For a spatially periodic system, a cluster is percolating if all its homologous points can be connected through the cluster.

A. Percolation threshold

In order to analyze the percolating probability of fractures with random surfaces for each value of the parameters of the model, N_r realizations were generated and the percolation probability P was defined as the fraction of realizations that contain a percolating cluster. The method used here to search for percolating and connected components of the void volume of a fracture is a modification of the method derived by Thovert, Salles, and Adler [32] for the characterization of the geometry of real porous media. Each node (x_i,y_j) is supposed to be connected with the first nearest neighbor in the x or y direction, but not with the second nearest neighbors $(x_{i\pm1},y_{j\pm1})$. First, connected components are determined, which contain nodes with $b>0$ that can be continuously connected through the cluster; then, nonpercolating clusters are eliminated by means of a pseudodiffusion process.

Thus the percolation of a fracture volume is considered here as a correlated site percolation problem with a site-occupation variable B_i defined on the discrete grid according to (28b). The site-occupation probability is equal to the mean value $\langle S_0\rangle$ given by (28c). The spatial correlation of $w(x,y)$ induces correlations of the occupation variables B_i. A similar approach to the correlated site percolation was developed by Prakash *et al.* [35], who considered normally distributed correlated fields converted to corresponding discrete correlated occupation variables.

1. Uncorrelated fields

The percolation probability P is analyzed as a function of the distance b_m/σ_h of the discretization ratio a/l and of the sample size L/l. First, P is calculated for uncorrelated fields $l=0$ to analyze the influence of $N_L=L/a$.

Figure 15 shows variations of P with b_m/σ_h for various values of N_L. The probability P increases monotonically from 0 to 1 when b_m/σ_h increases. The transition zone decreases when N_L increases; it should be a step function for infinite N_L.

The finite-size scaling method may be used in order to determine the percolation threshold P_c [36]. $P(S_0)$ is tentatively fitted by a two-parameter error function

$$P=\frac{1}{2\pi}\int_{-\infty}^{S_0}\frac{1}{\Delta}\exp\left\{-\frac{(\xi-P_{\mathrm{av}})^2}{2\Delta^2}\right\}d\xi, \tag{60}$$

where P_{av} is the average concentration and Δ is the width of the transition region [22]. The percolation threshold P_c is the limit for P_{av} when the sample size N_L tends to infinity. The critical exponent ν and P_c can be derived by using the scaling laws [22]

$$P_{\mathrm{av}}-P_c\sim N_L^{-1/\nu}, \tag{61a}$$

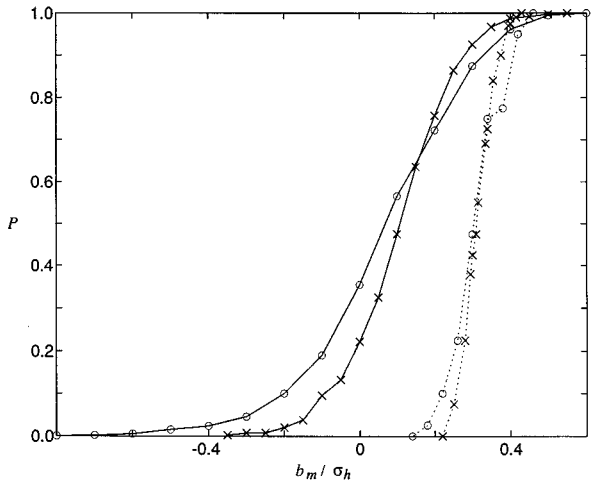

FIG. 15. Percolation probability P as a function of b_m/σ_h for correlated (solid lines) and uncorrelated (dotted lines) fields. Data are for $a/L=0.0167$ (○) and 0.01 (×). The correlated fields are generated with $H=0.5$, $l/a=2$.

$$\Delta\sim N_L^{-1/\nu}. \tag{61b}$$

Figure 16(a) shows a log-log plot of Δ vs N_L for a classical uncorrelated site percolation. Error bars are estimated by comparing P_{av} and Δ found with successive data points removed from the set (P,S_0). The linear fit gives $\nu=1.35\pm0.02$, which is close to the theoretical value 1.333. The percolation threshold P_c estimated by extrapolation of (61a) gives $P_c=0.59\pm0.04$, which is also close to the theoretical prediction 0.592 75 [Fig. 16(b)].

2. Correlated fields

The influence of the spatial correlations in the distribution of site-occupation variable B_i on the percolation threshold P_c was studied by various models [37,38,37,39,40]. Prakash *et al.* [35] and Sahimi [40] studied two-dimensional lattices with the site-occupancy variable B_i obtained by using random Gaussian fields u_i, which are described by correlation functions with ferro-type and antiferro-type correlations, respectively. The spatial correlations were introduced by using a power-law correlation function $C_u\sim r^{-2+\lambda}$, $-2<\lambda<2$ [35], and by generating a fractional Brownian motion with $C_u\sim 1-r^{2H}$, $0<H<1$ [40]. The systems with ferro-type correlations, when the neighbor of an occupied site prefers to be occupied, are represented in these models by $\lambda>0$ and $H>\frac{1}{2}$, respectively; the percolation threshold of such systems was shown to systematically decrease if the degree of spatial correlations, characterized by λ and H, increases.

Coniglio *et al.* [39] considered percolation in continuum systems using a Ising model of ferromagnets. A ferromagnetic interaction among particles introduces a spatial correlation that depends upon temperature. When temperature tends to infinity, the percolation threshold tends to the same threshold as for uncorrelated systems. Near but above the critical temperature, the correlation length of the system diverges and the percolation threshold tends toward $\frac{1}{2}$.

Weinrib [38] studied the percolation thresholds of a two-dimensional continuum system whose site-occupation variable $B(\mathbf{x})$ is zero for $|A(\mathbf{x})|^2<I^*$ and one for $|A(\mathbf{x})|^2\geq I^*$;

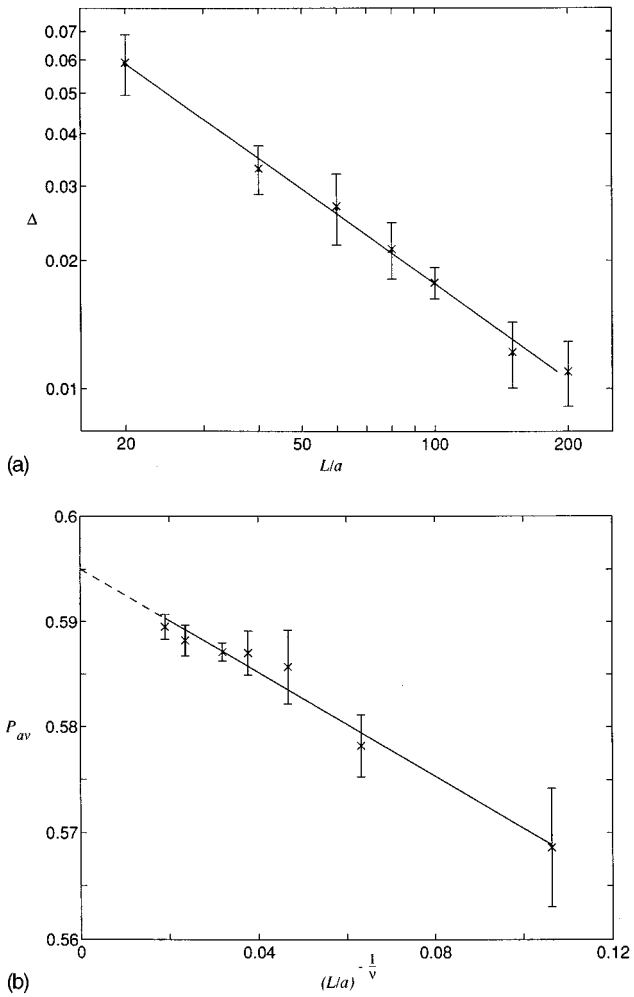

FIG. 16. (a) Width Δ of the transition region as a function of the sample size L/a for uncorrelated fields. The solid line corresponds to the linear fit of the numerical points with $\nu=1.34\pm0.02$. (b) Averaged concentration P_{av} as a function of the sample size $(L/a)^{-1/\nu}$ for uncorrelated fields. Data are for $\nu=1.337$. The linear fit (solid line) gives an extrapolated percolation threshold (dotted line) $P_c=0.59\pm0.04$.

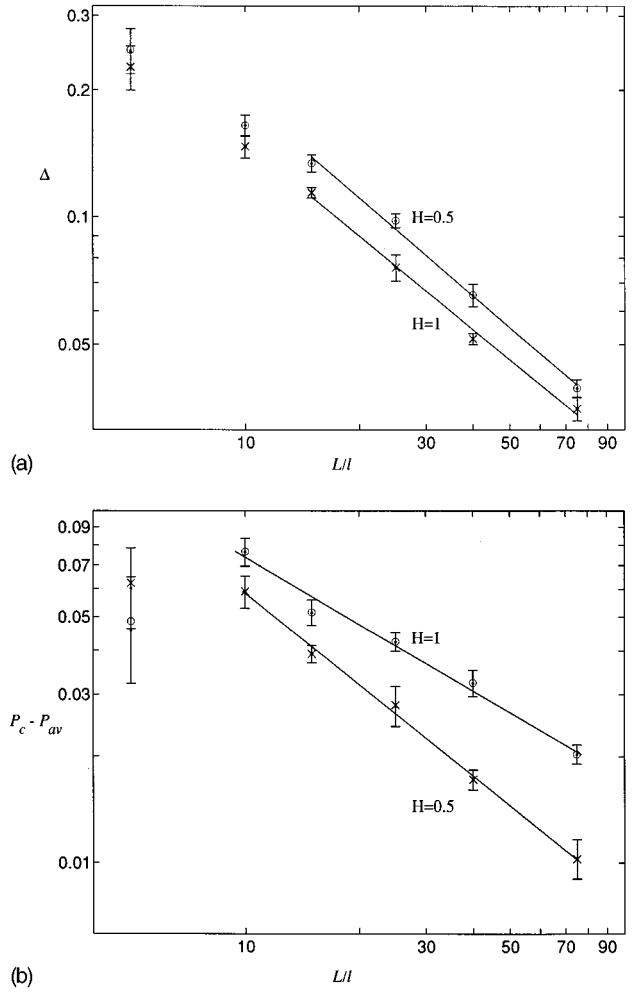

FIG. 17. (a) Width Δ of the transition region as a function of the sample size L/l for correlated fields. Data are for $a/l=0.25$. The solid lines are the least-squares fits of the numerical data points. The number of realizations is $N_r=800$ for $L/l=15$ and 200 for $L/l=75$. (b) Difference P_c-P_{av} as a function of the sample size L/l for correlated fields. Data are for $a/l=0.25$. The solid lines are the least-squares fits of the numerical data points.

$A(\mathbf{x})$ is a homogeneous, isotropic complex Gaussian random variable defined over the plane. He analyzed random fields on a discrete lattice with the Gaussian correlation function $\langle A(0)A^*(\mathbf{x})\rangle=I_0\exp(-x^2/2l^2)$ with $l/a=8$. The percolation threshold of such a system was found at $I^*/I_0=0.519$, which corresponds to $P_c=0.405$; this value is less than for a purely uncorrelated system $P_c\approx0.59$. It should be noted that this threshold differs from $\frac{1}{2}$, valid for many two-dimensional continuum systems with statistically equivalent conducting and insulating regions.

An analysis of the ''annealed percolation model'' [41], cubic resistor networks with correlated bonds [41], and percolation on random lattices [42] also showed that P_c is a decreasing function of the degree of spatial correlation within a percolating system. By using the technique of finite-size scaling, the percolation threshold P_c is analyzed here for correlated fields described by the correlation function (15). In this technique, the calculation of P_c follows the determination of the correlation-length exponent ν, but a detailed discussion of the results concerning ν will be presented in Sec. V B. The influence of two parameters on P_c is studied, namely, the discretization ratio a/l and the roughness exponent H.

The influence of spatial correlations on the percolation probability P is illustrated in Fig. 15. One can see that the transition region Δ is larger for correlated systems than for uncorrelated ones.

The two limits $a/l\gg1$ and $a/l\ll1$ correspond to two known situations, i.e., purely uncorrelated systems with $P_c=0.59$ and continuum systems with $P_c=1/2$ [38]. H has an effect similar to the Hurst exponent H in the model considered by Sahimi [40], because the correlation function (15) approximates $1-(r/l)^{2H}$ at $r/l\ll1$. In order to find the percolation threshold P_c and the exponent ν, P_{av} and Δ are calculated as functions of L/l for fixed ratios a/l. Figure 17 presents an example of numerical estimation of P_c and ν for $H=1$ and 0.5 and $a/l=0.25$. A trial value of P_c is used in order to obtain the best linear approximation of the log-log plot of P_c-P_{av} vs L/l; then, P_c is varied until a minimum mean-square difference between the linear fit and the nu-

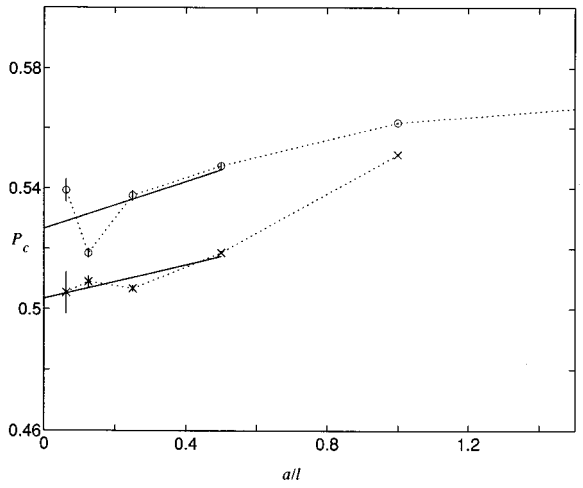

FIG. 18. Percolation threshold P_c as a function of the discretization ratio a/l. The solid lines are the least-squares fits of the numerical data points. Data are for $H=0.5$ (○) and 1 (×).

merical data is obtained. The finite-size scaling (61) gives $P_c \approx 0.507 \pm 0.001$ for $H=1$ and 0.538 ± 0.002 for $H=0.5$. The errors in P_c are estimated by successive removals of the data points from the set $(P_{\mathrm{av}}, L/l)$.

Figure 18 and Table IV provide the function $P_c(a/l)$ calculated for two values of H. In both cases, P_c is an increasing function of a/l. The percolation threshold P_c, calculated at $a/l=4$ for $H=0.5$, is equal to 0.5901 ± 0.0002, which is very close to the value of classical uncorrelated systems.

In the opposite limite $a/l \to 0$, linear extrapolations of the trends for $P_c(a/l)$ give $P_{c0} \approx 0.527 \pm 0.009$ and 0.503 ± 0.002 for $H=0.5$ and 1, respectively. Both values are close to $P_c = \frac{1}{2}$, which is valid for continuum systems. It should be noted that it is difficult to analyze the case of small a/l, because the mesh size N_L, which corresponds to a given effective sample size L/l, increases with decreasing a/l. The mesh size N_L is limited by computer time and memory and did not exceed 500, so only a relatively small range of L/l has been explored for small a/l.

TABLE IV. Percolation threshold P_c and the critical exponent ν as functions of the discretization ratio a/l for $H=1$ and 0.5.

a/l	P_c	ν
	$H=1$	
extrapolation	0.503 (0.002)	
0.0625	0.505 (0.007)	1.62 (0.01)
0.1250	0.509 (0.002)	1.43 (0.04)
0.2500	0.507 (0.001)	1.38 (0.03)
0.5000	0.519 (0.001)	1.35 (0.04)
1.0000	0.5519 (0.0007)	1.34 (0.04)
	$H=0.5$	
extrapolation	0.527 (0.009)	
0.0625	0.539 (0.004)	1.61 (0.04)
0.1250	0.519 (0.002)	1.36 (0.01)
0.2500	0.538 (0.002)	1.30 (0.04)
0.5000	0.547 (0.001)	1.33 (0.02)
1.0000	0.569 (0.002)	1.41 (0.06)
4.0000	0.590 (0.001)	1.37 (0.09)

A comparison of P_c for $H=0.5$ and 1 shows that it is smaller in the latter case; this agrees with the results of Sahimi [40], who found that P_c decreases with H. The percolation thresholds $P_c=0.5$ and 0.59 correspond to the mean contact areas $S_c=0.5$ and 0.41, respectively. Bandis, Lumsden, and Barton [43] measured S_c of various rock fractures under a normal load by inserting a thin plastic sheet between the interlocked joint walls; they found that S_c ranged between 0.4 and 0.7 for various samples at the largest pressures. Similar results were obtained by Gentier [2]. The resin injection in the fracture space under a normal load performed by Gale [15] gave $S_c=0.17$–0.18. Witherspoon *et al.* [44] measured S_c as 0.1–0.2 for granite samples and 0.25–0.35 for marble samples. Taking into account that the measurements using plastic films may overestimate S_c, one can see that the percolation threshold can be reached only at very high normal loads. This agrees with the fact that in most experimental works fractures remained open for fluid flow even at large pressures [2,15,44].

It would be interesting to use the percolation methods in the study of the hydromechanical behavior of fractures near the percolation threshold. It was shown [44] that the mean fracture aperture $\langle b \rangle$ and the hydraulic one b_h estimated during flow experiments are linearly related. This dependence is valid only at small and modest normal stresses. There are some experimental observations at large pressures [45], where b_h was found to decrease with $\langle b \rangle$ more rapidly than the linear dependence predicts. Pyrak-Nolte, Cook, and Nolte [46] attributed these deviations from the linear dependences between b_h and $\langle b \rangle$ to the behavior of the critical neck or the point of the smallest aperture along the flow path. This approach can be combined with standard methods of the percolation analysis [22] of the macroscopic conductivity near the percolation threshold in order to obtain the corresponding critical exponents and to compare them with the ones found in experiments. However, such an analysis is outside the scope of the present paper.

3. Analytical models

The existence of a diverging length scale in a percolating system near the percolation threshold provides the possibility of using the renormalization transformation in order to obtain the critical parameters [47,36,48]. The technique is based on the fact that the initial percolation system and the transformed one, whose sites replace finite cells of the initial lattice according to some cell-to-site transformation rule, display the same percolation properties. The spatial correlation of the site occupancy directly introduced in the system changes the situation. The properties of the percolation system at scales larger than the correlation distance l are expected to be similar to uncorrelated systems, but at small distances they depend on the correlation function, even near the percolation threshold. This means that the occupation probability of the renormalized site with size a_1 larger than l differs from that with $a_1 < l$ and the search for the fixed point of the renormalization transformation cannot give true value of P_c.

However, the renormalization procedure can be directly used in order to estimate global properties of the correlated

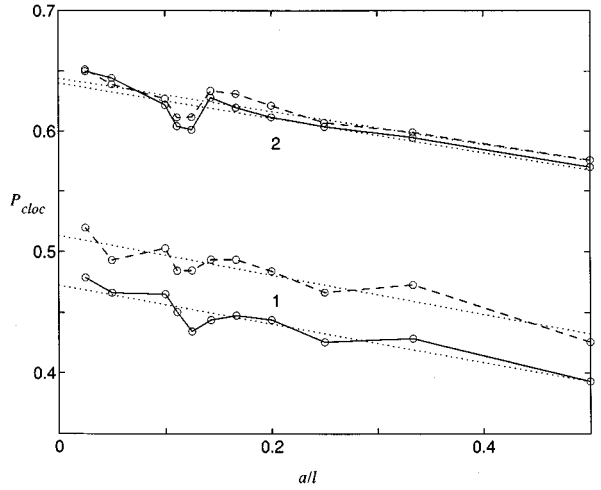

FIG. 19. Local percolation probability $P_{c\,\mathrm{loc}}$ as a function of a/l for $H=1$ (solid lines) and 0.5 (dashed lines) for the percolation in one direction and in two directions. Data are for $L/l=2$. The number of realizations is $N_r=100$ for the minimum a/l and 2000 for the maximum a/l.

systems [49]. It was shown that successive recalculations of permeabilities of a network with a small size unit cell to that with a larger one give the best global permeability estimate when compared to conventional averaging techniques, such as the geometric mean.

The fact that a correlated system should have the same critical parameters as an uncorrelated one at scales larger than l is used here in order to estimate the percolation threshold P_c in the limit $a/l\to 0$. If a renormalized site has a size $a_1>l$, it can be considered as a site of an uncorrelated percolating system with the known ''global'' percolation threshold $P_c\approx 0.593$. One can use a Monte Carlo renormalization-group procedure [36] to calculate a local site occupation probability $P_{c\,\mathrm{loc}}$, for which the fraction of large-scale percolating cells is equal to P_c. $P_{c\,\mathrm{loc}}$ will be referred to as a ''local'' percolation threshold.

A series of random correlated fields is generated on a grid of size $L_0/l=4$ and a square $L/l=2$ is cut from each sample. A percolation probability is calculated for various site probabilities S_0. The procedure that was used for large-scale percolation analysis is applied here to find the average concentration P_{av} and the width Δ. Using formula (60), the percolation threshold $P_{c\,\mathrm{loc}}$ is calculated.

A rule is chosen in order to decide whether or not a large cell is occupied. The renormalized cell is occupied if it percolates at least in one direction. Figure 19 shows $P_{c\,\mathrm{loc}}$ vs a/l calculated for $H=1$ and 0.5. It was difficult to avoid statistical errors in the estimation of $P_{c\,\mathrm{loc}}$ even with a relatively large number of realizations (more than 1000 for $a/l>0.2$). But, the trend is obvious; $P_{c\,\mathrm{loc}}$ decreases with a/l and tends toward a limit for small a/l.

The functions $P_{c\,\mathrm{loc}}$ (a/l) are fitted by linear functions and the limits for $a/l\to 0$ are estimated by extrapolation. Table V contains these limit values together with $P_{c\,\mathrm{loc}}$ calculated for $a/l=0.025$. The values $P_{c\,\mathrm{loc}}$, which are found by using the second rule (percolation in 1 direction), are close to the ones found in the global analysis (see Table IV).

TABLE V. ''Local'' percolation threshold $P_{c\,\mathrm{loc}}$ for various H and various percolation rules.

H	$P_{c\,\mathrm{loc}}$ $(a/l=0.025)$	$P_{c\,\mathrm{loc}}$ $(a/l=0)$
	one direction	
0.5	0.520	0.513
1	0.479	0.472
	two directions	
0.5	0.651	0.644
1	0.650	0.640

In both cases, the percolation threshold is less for $H=1$ than for $H=0.5$.

This approach implies that all sites in a large-scale sample are independent, which indeed is not true. The validity of these estimations may be analyzed by calculating the covariance of percolation probability C_p,

$$C_p=\frac{\langle P_iP_j\rangle-\langle P_i\rangle^2}{\langle P_i\rangle-\langle P_i\rangle^2}, \tag{62}$$

where $P_i=1$ if a cell percolates and 0 if not; P_i and P_j correspond to two neighbor cells cut from the same sample with $L_0=2L$. Figure 20 shows C_p calculated for $H=1$ and for the percolation along one direction. It is clear that within statistical errors, C_p can be considered as almost constant over a wide range of values of S_0, except close to 0 or 1. For $a/l=0.5$, the covariance C_p is about 0.2 and increases up to 0.4–0.5 when a/l decreases down to 0.05. This means that the correlations between neighboring sites remain significant and can influence the percolation threshold $P_{c\,\mathrm{loc}}$. Calculations performed for $H=0.5$ and for the percolation in two directions show that the maximal value of C_p is not changed.

The covariance C_p decreases if the renormalized cells have a size L/l larger than 2. Figure 21 shows C_p calculated

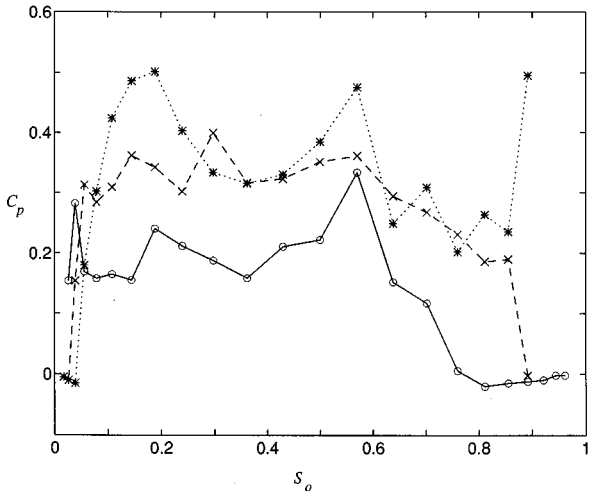

FIG. 20. Covariance C_p of the percolation probabilities as a function of the ''site'' probability S_0 for the percolation along one direction. Data are for $H=1$, $N_r=100$, and $L/l=2$. The solid line corresponds to $l/a=2$, the dashed line to $l/a=8$, and the dotted line to $l/a=20$.

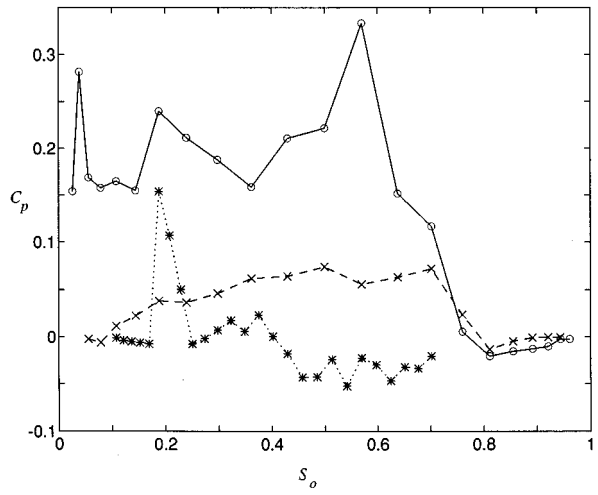

FIG. 21. Covariance C_p of the percolation probabilities as a function of the site probability S_0 for the percolation along one direction. Data are for $H=1$ and $L/l=2$. The solid line corresponds to $L/l=2$, the dashed line to $L/l=4$, and the dotted line to $L/l=8$.

for three successive values of L/l. For $L/l=4$, C_p is less than 0.06 and such sites can be considered as uncorrelated.

B. The critical exponent ν

Near the percolation threshold P_c, the connectivity length ξ_p, which is defined as the average root-mean-square distance between occupied sites belonging to the same finite cluster [31], diverges as [22]

$$\xi_p \sim |p-P_c|^{-\nu}, \tag{63}$$

where ν is the critical exponent. It was shown that for various percolation systems without any spatial correlation, ν is almost the same [36].

However, there are some situations where long-range correlations affect the critical properties. Weinrib [50] studied the correlated percolation problem with a power law correlation function $C_B \sim r^{-\alpha}$. He supposed that a uniform transition takes place across the system if the spatial variations of $(1/V)\Sigma_{i\in V}B_i$ for different regions V are small compared to $p-P_c$; he found that the scaling law (63) with the same correlation exponent ν as for pure random system is valid only if $\alpha>2/\nu$ for two-dimensional percolation. Systems with $\alpha<2/\nu$ exhibit a new critical behavior with

$$\nu^* = 2/\alpha. \tag{64}$$

Prakash *et al.* [35] used a Monte Carlo renormalization-group calculation applied to a correlated percolation problem with power-law correlations. They found that the calculated ν agrees with (64) for $\alpha>1$. For $\alpha\leqslant 1$, their values of ν were lower than the predictions of (64).

The study of the effect of the correlated percolation problem on systems whose occupancy variables are obtained by fractional Brownian motion with $C_u \sim 1-r^{2H}$ showed that for all H, the critical exponent ν retains its value for uncorrelated systems [40]. The same result was obtained in the analysis of annealed correlated percolation [39].

The finite-size scaling method is applied here to the percolation problem in correlated systems with covariance functions $C_h(r)$ given as power laws

$$C_h(r_i) = \sigma_h^2 \begin{cases} \dfrac{1}{2-2^{-\alpha}} \left(\dfrac{r_i}{a}\right)^{-\alpha}, & i=1,\ldots,N_L/2 \\ 1, & i=0, \end{cases} \tag{65}$$

where $\alpha=1$ and 3. It can be shown that near the percolation threshold the correlation function $C_B \approx (2/\pi)\arcsin(C_h/\sigma_h^2)$ and decreases at $r\to\infty$ with the same exponent α as C_h. The critical exponent ν is estimated by the error function, which fits (60) for numerical data and the power law (61b). It was found that $\nu=1.35\pm0.02$ for $\alpha=3$ and $\nu=2.26\pm0.02$ for $\alpha=1$. One can see that the long-range spatial correlations in the site occupations described by the power law (65) influence the critical behavior of the percolation system. The value $\nu=2.26$ is larger than $\nu=2$ given by (64), which can be explained by the high sensitivity of ν to statistical errors.

The same finite-size scaling method is used for the percolation systems described by the covariance functions (15). The critical exponent ν is calculated for $H=0.5$ and 1 and various values of the discretization ratio a/l. One may expect that the correlation systems with an exponentially decreasing covariance function (15) have no long-range correlations and exhibit the same critical behavior near the percolation threshold as uncorrelated systems. Table IV presents values of ν estimated for $H=0.5$ and 1 and it can be seen that ν indeed varies near its value $\nu=1.333$ for classical uncorrelated percolating systems. No substantial influence of a/l on ν was observed.

C. The critical exponent β

It is known that near the percolating threshold $S_0 \sim P_c$, the mean fraction area $\langle S_{\mathrm{PC}}\rangle$ of the percolating cluster for infinite systems depends on $\langle S_0\rangle$ as

$$\langle S_{\mathrm{PC}}\rangle \sim (\langle S_0\rangle - P_c)^{\beta}, \tag{66}$$

where β is a critical exponent; for two-dimensional systems, it is equal to

$$\beta = \tfrac{5}{36} \approx 0.139 \tag{67}$$

for all types of lattice structures with noncorrelated elements.

It is difficult to calculate β directly for correlated systems because it is very sensitive to various factors. Instead of β, the finite-size scaling technique is used, which provides the ratio β/ν.

For finite lattices, the percolating cluster area S_{PC} depends not only on S_0, but also on the size of the system. Near the percolation threshold, $\langle S_{\mathrm{PC}}\rangle$ for noncorrelated finite systems of size L verifies [22]

$$\langle S_{\mathrm{PC}}\rangle \sim L^{-\beta/\nu} F([\langle S_0\rangle - P_c]L^{1/\nu}), \tag{68}$$

where ν is the critical exponent and F is a scaling function. For fixed $\langle S_0\rangle$ and varying L [so that $(\langle S_0\rangle - P_c)L^{1/\nu} \ll 1$], $\langle S_{\mathrm{PC}}\rangle$ is proportional to $L^{-\beta/\nu}$; for two-dimensional lattices

$$\frac{\beta}{\nu} = \frac{5}{48} \approx 0.104. \tag{69}$$

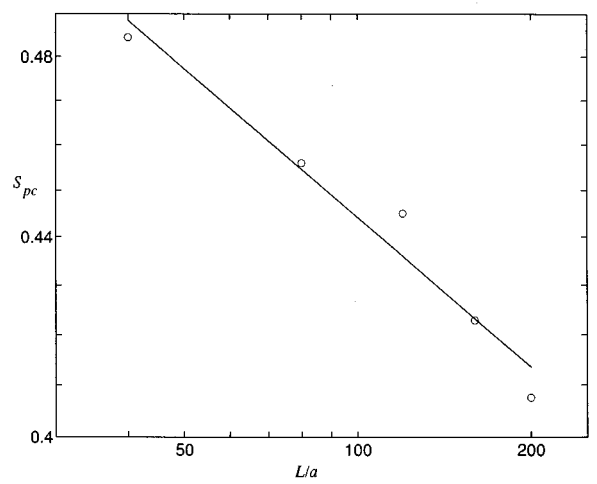

FIG. 22. log-log plot of the strength $\langle S_{\mathrm{PC}}\rangle$ of the percolating cluster in the noncorrelated lattice as a function of the lattice size L/a for the site probability $P_c=0.593$. The solid line corresponds to the linear fit of the numerical data.

Figure 22 displays a log-log plot of $\langle S_{\mathrm{PC}}\rangle$ vs the system size L/a for an uncorrelated lattice. The site occupation probability is $\langle S_0\rangle \approx 0.593$. A linear fit gives $\beta/\nu=0.103$ (0.01), which is in good agreement with (69).

For correlated fields, the following approach is used. The discretization ratio l/a is fixed and the separation b_m/σ_h is chosen so that the site probability $\langle S_0\rangle$ is equal to the percolation threshold P_c for given l/a and H. Then, L/l is varied and $\langle S_{\mathrm{PC}}\rangle$ is estimated. Figure 23 shows log-log plots of $\langle S_{\mathrm{PC}}\rangle$ vs L/l for $H=0.5$ and 1 and $l/a=8$. The ratio β/ν is derived from the slope of the linear fit of the numerical data. Table VI presents values of β/ν for $H=0.5$ and 1 and various values of l/a. One can see that for $H=1$ the ratio β/ν is almost the same as for uncorrelated lattices. In the case $H=0.5$, β/ν increases slightly with l/a from 0.073 for $l/a=1$ up to 0.13 for $l/a=8$.

The difference between $H=0.5$ and 1 can be explained if

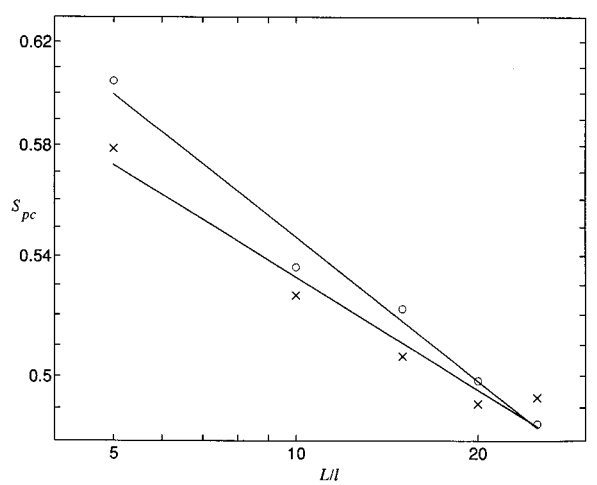

FIG. 23. log-log plot of the strength $\langle S_{\mathrm{PC}}\rangle$ of the percolating cluster in correlated systems as a function of the effective lattice size L/l for $l/a=8$. Solid lines correspond to the linear fit of the numerical data. Data are for $H=1$, $b_m/\sigma_h=0.06$ (○) and $H=0.5$, $b_m/\sigma_h=0.13$ (×).

TABLE VI. Critical exponent β and the ratio β/ν for $H=0.5$ and 1 and for various l/a. The exponent β is derived from the ratio β/ν and the value of ν in Table IV.

a/l	β/ν	β
	$H=1$	
0.1250	0.10 (0.01)	0.15 (0.02)
0.2500	0.12 (0.02)	0.16 (0.03)
0.5000	0.096 (0.008)	0.13 (0.02)
1.0000	0.099 (0.008)	0.13 (0.02)
4.0000	0.12 (0.01)	0.16 (0.02)
	$H=0.5$	
0.1250	0.13 (0.01)	0.18 (0.02)
0.2500	0.11 (0.01)	0.14 (0.02)
0.5000	0.09 (0.01)	0.12 (0.02)
1.0000	0.073 (0.007)	0.10 (0.02)

one takes into account that the void zone of the fracture is a fractal in the first case. This means that the scaling properties of the percolating cluster near the percolation threshold may be influenced by the internal geometric structure of a fractal.

For $l/a=1$ and $H=0.5$, it is found that β/ν is smaller than the value given in (69). This is surprising because one may expect that when l/a tends to 0, the system becomes uncorrelated. Hence these results show that the scaling properties of the percolating cluster in correlated systems may depend upon the form of the spatial correlation in site occupations.

D. The critical exponent γ

Consider the average size of the void zones Z_0 defined by Eq. (24). Near the percolation threshold, $\langle Z_0\rangle$ depends on $\langle S_0\rangle$ as [22]

$$\langle Z_0\rangle \sim |\langle S_0\rangle - P_c|^{-\gamma}, \tag{70}$$

where γ is a critical exponent.

It is difficult to obtain γ directly and again finite-size scaling is used. The method is based on the expected scaling behavior of $\langle Z_0\rangle$, which should increase with L/l as

$$\langle Z_0\rangle \sim \left(\frac{L}{l}\right)^{\gamma/\nu}. \tag{71}$$

For fixed values of l/a, $N_r=200$ realizations of correlated fields were generated and the mean size $\langle Z_0\rangle$ is calculated and averaged over nonpercolating configurations. The ratio γ/ν is calculated from a linear fit of the log-log plot of $\langle Z_0\rangle$ vs L/l. Figure 24 displays $\langle Z_0\rangle$ as a function of L/l for uncorrelated fields estimated at $\langle S_0\rangle=0.593$. A linear fit of the numerical data gives the ratio $\gamma/\nu=1.88$ (0.05), which is close to the theoretical value

$$\frac{\gamma}{\nu}=\frac{43}{24}\approx 1.7917. \tag{72}$$

Calculations of $\langle Z_0\rangle$ for correlated systems were performed only for small l/a. For large l/a (>4), the dependence of $\langle Z_0\rangle$ upon L/l is significantly different from (71) due to the statistical scatter of the numerical data and a cor-

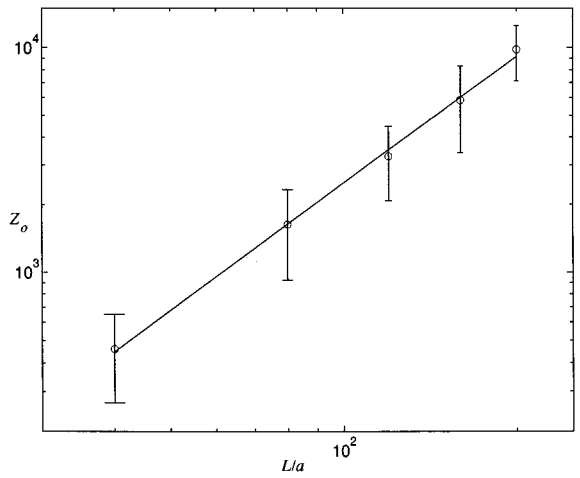

FIG. 24. Mean finite cluster size $\langle Z_0 \rangle$ in noncorrelated lattices as a function of the lattice size L/a for the site probability $P_c=0.593$. The solid line corresponds to the linear fit of the numerical data. The error bars represent the standard deviation of Z_0.

rect estimation of the ratio γ/ν was impossible. For $l/a=1$, linear fits of log-log plots $\langle Z_0 \rangle$ vs L/l gave the same ratio $\gamma/\nu=1.87$ (0.06) for both $H=0.5$ and 1. In the case $H=1$ and $l/a=4$, the value $\gamma/\nu=1.93$ (0.03) was found. Hence the numerical analysis of the scaling behavior of the mean cluster size $\langle Z_0 \rangle$ does not reveal any influence of the spatial correlations on the ratio γ/ν.

VI. CONCLUDING REMARKS

The geometry of simulated fractures has been analyzed by using numerical and analytical methods. A fracture was presented as a space between two random surfaces described by a normal probability distribution of heights and a spatial covariance function in the fracture plane. The numerical results, relative to the mean area of contacts between the surfaces of the fracture, the mean aperture, and the expected number of contacts, have been successively compared to analytical expressions for various values of the distance between the surfaces and of the correlation length. The mean contact number for fractures with a spatially correlated height profile distribution is found to depend on the discretization ratio according to a power law. It was shown that the percolation threshold for the model of a fracture considered corresponds to the site percolation on a square lattice. The percolation threshold for a correlated system is smaller than that in a pure random lattice. Near the percolation threshold, the percolating cluster (which is formed by the open space of the fracture) has fractal scaling properties and the critical exponents for various values of the parameter H in the covariance function of the generated surfaces profile were estimated.

[1] I. Ippolito, P. Kurowski, G. Daccord, and J. P. Hulin (unpublished).
[2] S. Gentier, Doctoral thesis, Université d'Orléans, 1986 (unpublished).
[3] Y. W. Tsang and C. F. Tsang, Water Resour. Res. **25**, 2076 (1989).
[4] S. B. Brown, J. Geophys. Res. **92**, 1337 (1987).
[5] H. Abelin, L. Birgersson, J. Gidlund, and I. Neretnieks, Water Resour. Res. **27**, 3107 (1991).
[6] L. Moreno, Y. W. Tsang, C. F. Tsang, F. V. Hale, and I. Neretnieks, Water. Res. Res. **34**, 2033 (1988).
[7] L. Moreno and I. Neretnieks, J. Contaminant Hydrol. **13**, 49 (1993).
[8] Y. W. Tsang and P. A. Witherspoon, J. Geophys. Res. **88**, 2359 (1983).
[9] S. R. Brown and C. H. Scholz, J. Geophys. Res. **91**, 4939 (1986).
[10] D. L. Hopkins, N. G. W. Cook, and L. R. Myer, in *Rock Joints* (Balkema, Rotterdam, 1990), pp. 203–210.
[11] S. R. Brown, R. L. Kranz, and B. P. Bonner, Geophys. Res. Lett. **13**, 1430 (1986).
[12] S. R. Brown and C. H. Scholz, J. Geophys. Res, **90** 12 575 (1985).
[13] E. Hakami and N. Barton, in *Rock Joints* (Ref. [10]), pp. 383–390.
[14] E. Hakami (unpublished).
[15] J. E. Gale (unpublished).
[16] S. R. Brown, J. Geophys. Res. **94**, 9429 (1989).
[17] A. J. A. Unger and C. W. Mase, Water Resour. Res. **29**, 2101 (1993).
[18] J. S. Y. Wang, T. N. Narasimhan, and C. H. Scholz, J. Geophys. Res. **93**, 2216 (1988).
[19] F. Plouraboué, P. Kurowski, J.-P. Hulin, S. Roux, and J. Schmittbuhl, Phys. Rev. E **51**, 1675 (1995).
[20] R. J. Adler, *The Geometry of Random Fields* (Wiley, Chichester, 1981).
[21] L. K. Barrett and C. S. Yust, Metallography **3**, 1 (1970).
[22] D. Stauffer and A. Aharony, *Introduction to Percolation Theory*, 2nd ed. (Taylor and Francis, Bristol, 1994).
[23] P. M. Adler, *Porous Media: Geometry and Transports* (Butterworth/Heinemann, Stoneham, MA, 1992).
[24] S. R. Brown and C. H. Scholz, J. Geophys. Res. **90**, 5531 (1985).
[25] D. J. Whitehouse and J. F. Archard, Proc. R. Soc. London Ser. A **316**, 97 (1970).
[26] E. Hakami and E. Larsson (unpublished).
[27] S. K. Sinha, E. B. Sirota, S. Garoff, and H. B. Stanley, Phys. Rev. B **38**, 2297 (1988).
[28] B. B. Mandelbrot, *The Fractal Geometry of Nature* (Freeman, San Francisco, 1983).
[29] E. Bouchaud and J.-P. Bouchaud, Phys. Rev. B **50**, 17 752 (1994).
[30] R. Gutfraind, I. Ippolito, and A. Hansen, Phys. Fluids **7**, 1938 (1995).
[31] J. Feder, *Fractals* (Plenum, New York, 1988).
[32] J. F. Thovert, J. Salles, and P. M. Adler, J. Microsc. **170**, 65 (1993).
[33] P. M. Adler, C. C. Jacquin, and J. Quiblier, Int. J. Multiphase Flow **16**, 691 (1990).

[34] B. B. Mandelbrot, Proc. Natl. Acad. Sci. U.S.A. **72**, 3825 (1975).
[35] S. Prakash, S. Havlin, M. Schwartz, and H. E. Stanley, Phys. Rev. A **46**, R1724 (1992).
[36] P. J. Reynolds, H. E. Stanley, and W. Klein, Phys. Rev. B **21**, 1223 (1980).
[37] A. Coniglio, C. R. Nappi, F. Peruggi, and L. Russo, J. Phys. A **10**, 205 (1977).
[38] A. Weinrib, Phys. Rev. B **26**, 1352 (1982).
[39] D. A. Wollman, M. A. Dubson, and Q. Zhu, Phys. Rev. B **48**, 3713 (1993).
[40] M. Sahimi, J. Phys. (France) I **4**, 1263 (1994).
[41] I. Webman, J. Jortner, and M. H. Cohen, Phys. Rev. B **11**, 2885 (1975).
[42] G. E. Pike and C. H. Seager, Phys. Rev. B **10**, 1421 (1974).
[43] S. C. Bandis, A. C. Lumsden, and N. K. Barton, Int. J. Rock Mech. Min. Sci. **20**, 249 (1983).
[44] P. A. Witherspoon, J. S. Y. Wang, K. Iwai, and J. E. Gale, Water Resour. Res. **16**, 1016 (1980).
[45] J. E. Gale (unpublished).
[46] L. J. Pyrak-Nolte, N. W. Cook, and D. D. Nolte, Geophys. Res. Lett. **15**, 1247 (1988).
[47] R. B. Stinchcombe and B. P. Watson, J. Phys. C **9**, 3221 (1976).
[48] M. Sahimi, B. D. Hughes, L. E. Scriven, and H. T. Davis, Phys. Rev. B **28**, 307 (1983).
[49] E. L. Hinrichsen, A. Aharony, J. Feder, A. Hansen, T. Jøssang, and H. H. Hardy, Transp. Porous Media **12**, 55 (1993).
[50] A. Weinrib, Phys. Rev. B **29**, 387 (1984).